Spring 4-22-2016

IMPROVING RADIATION AND STRESS CORROSION CRACKING RESISTANCE OF AUSTENITIC STAINLESS STEELS BY LASER SHOCK PEENING

Qiaofeng Lu
University of Nebraska-Lincoln, qiaofeng.lu@huskers.unl.edu

IMPROVING RADIATION AND STRESS CORROSION CRACKING RESISTANCE OF AUSTENITIC STAINLESS STEELS BY LASER SHOCK PEENING

by

Qiaofeng Lu

A THESIS

Presented to the Faculty of

The Graduate College at the University of Nebraska

In Partial Fulfillment of Requirements

For the Degree of Master of Science

Major: Mechanical Engineering and Applied Mechanics

Under the Supervision of Professor Bai Cui

Lincoln, Nebraska

May, 2016

IMPROVING RADIATION AND STRESS CORROSION CRACKING RESISTANCE OF AUSTENITIC STAINLESS STEELS BY LASER SHOCK PEENING

Qiaofeng Lu, M.S

University of Nebraska 2016

Advisor: Bai Cui

Structural alloys for Generation-IV nuclear reactors need to endure a high neutron dose, high temperature, and corrosive coolant. Austenitic stainless steels, particularly the oxide-dispersion-strengthened (ODS) austenitic steels, are promising candidate materials, but they suffer several limits such as irradiation damage and stress corrosion cracking (SCC). This research applies a laser shock peening (LSP) process to improve the radiation and SCC resistance of austenitic stainless steels in simulated nuclear reactor environments. A high density dislocation networks, stacking faults and twin boundaries were generated in the surface region of 304 steels by the shock wave-material interactions in the LSP process. In-situ TEM irradiation experiments suggest that laser-peened 304 steels suffer less radiation damage than the untreated samples because the generated dislocation networks and twin boundaries serve as sinks for the annihilation of irradiation defects. Stress corrosion cracking tests show that transgranular cracks propagate in the untreated 304 steels, while no apparent cracks were observed in laser peened 304 steel samples on the same conditions.

ACKNOWLEDGEMENTS

I would like to express my special gratitude to my committee chair, Professor Bai Cui and my committee members, Professor Jeffery Shield and Professor Michael Nastasi. I appreciate all the comments, discussions and suggestions you have given on my research and thesis.

It is my pleasure to acknowledge the staff at the Argonne National Lab, Dr. Meimei Li, Dr. Mark Kirk, Pete Baldo and Ed Ryan for offering me the technical supports in the Intermediate Voltage Electron Microscopy (IVEM)-Tandem Facility.

I would also like to thank the staff at the Nebraska Center for Materials and Nanoscience (NCMN) at University of Nebraska Lincoln for all the trainings and efforts to keep the facility maintained in good conditions for my research.

I am also indebted to my colleague Fei Wang in my research group for the generous help and countless advice throughout my research and study. It is always a great time working and having discussions with you! Thank you and thank all the people who help me during my graduate study and research.

In the end, I owe my sincere gratitude to my family, who served as a solid foundation in my life and provided countless supports for my graduate study. I could not go this far without you!

TABLE OF CONTENTS

LIST OF FIGURES

CHAPTER 1: INTRODUCTION AND BACKGROUND

1.1 Motivation

Generation IV nuclear reactors are one of the most promising power sources for the energy crisis in the upcoming decades. The safe, efficient and long-term operational life of this new generation nuclear plant brings about a higher demand of the structural materials, which include the enduring of higher neutron doses, higher operation temperatures and extremely corrosive coolants. One of the currently used structural materials in the light water reactors and pressurized water reactors are austenitic stainless steels. The greatest problems that limit their operational life are the long-term radiation damage and stress corrosion cracking.

To address the above problems, one possible solution is to develop new material. Oxide-dispersion-strengthened (ODS) alloys are one of the promising candidate materials. By introducing the dispersed oxide nanoparticles (< 10nm) in the alloy matrix, excellent radiation tolerance and high temperature creep resistance can be obtained. However, ODS austenitic alloys are also susceptible to stress corrosion cracking in primary and supercritical water environments.

One potential solution is the laser shock peening (LSP). Studies found that many metallic materials exhibit enhanced mechanical properties including toughness, tensile strength and hardness after subjected to LSP. In order to obtain deeper insights of its mechanism and the LSP effect, laser shock peening process was performed on both 304

and 304 ODS stainless steels followed by microstructural characterization, in-situ irradiation transmission electron microscopy and stress corrosion cracking test.

1.2 Austenitic Stainless Steels and Oxide-Dispersion-Strengthened Steels

Austenitic stainless steels are the most common types of stainless steels. The austenite phase is face-center cubic (FCC) structure which leads to the high toughness, ductility and formability of the austenitic stainless steels. Typical compositions of austenitic stainless steels include chromium and nickel. The addition of chromium can increase the strength and most importantly, increase the resistance against corrosion of the steels and the addition of nickel serves the function of stabilizing the austenite phase of the steel. One weakness of austenitic stainless steels is their low strength compared to other types of steels, but they can be easily strengthened by cold-working such as rolling, drawing, bending or shearing. Another weakness is their susceptibility to stress corrosion cracking (SCC). Since many of the structural steels are used in a stress and corrosive environment, this SCC problem can greatly lower their operational life and increase the cost [1].

In contrast to the traditional stainless steels, oxide-dispersion-strengthened (ODS) steels, especially the ODS austenitic stainless steels are among the most promising structural materials. One application of ODS austenitic stainless steels is as structural materials for the Generation IV nuclear power plants. ODS austenitic stainless steels are known to exhibit excellent mechanical properties such as high strength, long fatigue life, low creep at high temperature etc. and the extraordinary high resistance against radiation

damage. These exceptional properties of ODS austenitic steels originate from the nano-size oxide particles. Yttrium oxide and yttrium-titanium oxide are commonly used to prepare ODS steels because of its high strength and high thermal stability and Figure 1.1 shows the morphology of Y_2O_3 nano-size particles distributed in the ODS 316 stainless steels. The principle is that the uniform distributed nano-size oxide particles can serve as obstacles against dislocation motion. With that, a higher stress is needed in order to produce plastic deformation. In the meantime, since these particles are thermally stable, a high temperature creep resistance can be obtained. In addition, introducing these nano-size oxide particles can generate interfaces between the particles and the base material – these interfaces can serve as sinks for radiation defects [2-4].

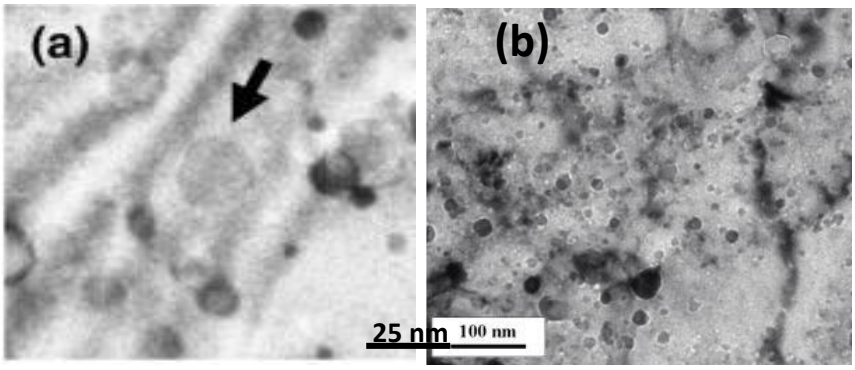

Figure 1.1 Morphology of the nano-size oxide particles in the austenitic steel matrix. (a) is the Y_2O_3 in 316 ODS steel. (b) is the $Y_2Ti_2O_7$ in 304 ODS steel [3,4]

1.3 Laser Shock Peening

1.3.1 Principle of Laser Shock Processing

Laser shock peening, also known as laser shock processing was first discovered in early 1960s and now is developed as a novel cold-working method for surface modification [5-7]. Prior to the discovery and development of laser shock processing, shot peening is the dominating surface modification method to induce compressive residual stress and to improve mechanical properties by cold-working. The limitations of shot peening process are obvious, including its instability of the peening energy, low affected depth and rough surface finish. As a result, when laser shock processing was first found with the advantages of stable energy and well surface finish, it kindled the interest of many scientists. Subsequent researches successfully improved the energy intensity, depth of affected zone as well as many other aspects of this technique and made it possible to induce residual compressive stress and plastic deformation of the material while maintaining a smooth surface finish [8-14].

The Q-switched laser pulse with the yttrium aluminum garnet (YAG) crystal lasing rod is commonly used for research purpose because of its low cost, high efficiency and reliability. Compared with other sources, the Q-switched source has the characteristics of high energy intensity and short duration time, which are advantageous for producing shock waves. The mechanism of shock wave generation and propagation have been studied and can be simplified in Figure 1.1[3] below: it started as the laser pulse hits the material, because of the high energy intensity of the laser source, material will vaporize

and form a plasma on its top. A plasma consists of high temperature gas with large numbers of electron charges. Depending on the relative number of positive ions versus negative charges, a plasma can be positively, negatively charged and neural. In the case of laser shock peening, the plasma is composed by high temperature vaporized gas with an equal number of positive ions and negative electrons. As a result, this generated plasma can expand by continuously absorbing the laser energy and embracing the vaporized material. A pressure as high as several hundred GPa can thus be exerted on the surface of the material and produce a stress field. In this way, the absorbed laser energy converts into mechanical energy and can finally transport to the material in the form of shock waves. When the shock wave accumulates to a point that the stress field produced by it exceeds the yield strength of the material, plastic deformation occurs. In the meantime, as shock wave can propagate to the interior of the sample, plastic deformation can take place several millimeter depth from the surface.

Note Figure.1 that there is a sacrificial coating and a transparent overlay on top of the sample. Both of them are designed to enhance intensity of the shock wave and facilitate its propagation. The function of the sacrificial layer is to protect the material from melting and ablation which are disadvantageous to the formation of plasma as well as the surface finish. Two common types of sacrificial coatings are metallic coating and organic coating. The former one uses metal with high melting point and excellent heat conductivity such as aluminum, zinc and copper. The latter one is proved to have higher thermal absorption and be beneficial to the smooth surface finish. The transparent overlay works as a confinement of the plasma region from the over-expanding. In other words,

this overlay keeps a high concentration of plasma and ensures enough amount of laser energy be transported to the material and generates shock wave. In practice, flowing water is used as the overlay in most of the laser processing system [15].

During the operation of laser shock processing, the following parameters have significant impacts to the peening effect and need to be adjusted in accordance to different material systems: spot size, laser energy, duration time, overlap rate, wavelength of the laser beam and beam profile.

Spot size is the diameter of the laser beam, which relates to energy density of the laser beam and can range from less than 1mm to as large as 5 mm. P. Pevre el at. along with a finite element analysis discovered the affected depth of the plastic deformation increased by 20% when the spot size increased from 0.5mm to 4mm [16,17] . D. Kan and Y. Lin also found that residual stress generated by laser processing increase from 300 MPa to 400 MPa by increasing the spot size from 1 mm to 4 mm [17]. As for the Q-switch Nd:YAG laser source, however, the maximum spot size can only be 1 mm. Duration time refers to the intervals between each laser pulse, which can be several nanosecond to one hundred nanosecond. The typical duration time of the Q-swtich:YAG system is less than 10ns. Overlap rate is an important factor when performing multiple times laser shock peening. Since it is difficult and time consuming to manipulate the laser beam to arrive at the same location for multiple times peening, overlap rate is introduced to describe how much percentage of the peening area overlaps with the previous one. Common overlap rates are 50%, 75% and 90%. In most cases, with the increase of overlap rates, the laser peening effect increases until a saturation point is reached.

1.3.2 Laser Shock Processing Effect on Inducing Compressive Residual Stress

One effect of the laser shock processing is the introduction of compressive residual stress, which is perpendicular to the direction of the propagating shock wave. Many studies have been carried out to determine the laser shock processing generated residual stresses both on the surface and along the depth of the sample. The most commonly used technique for residual stress measurement is called $\sin^2\psi$ X-ray diffraction method. Advantages of this method include: non-destructive, large depth penetration of X-ray (about 10 micron) as well as controlled area or local region. The principle of this measurement is the induced stress (compressive or tensile) will change the spacing of the crystal plane or d-spacing of the material and this will generate an angle ψ between the sample surface normal and lattice plane normal as shown in Figure 1.2 below. This angle ψ along with the Bragg angle 2Θ are related to the stress value б by the following equation:

$$\sigma = -\frac{E}{2(1+v)} \cdot cot\theta_0 \cdot \frac{\pi}{180} \cdot \frac{\Delta(2\vartheta)}{\Delta(sin^2\varphi)} = K \cdot \frac{\Delta(2\theta)}{\Delta(sin^2\varphi)} \qquad \text{Eqn. 1}$$

where E is the Young's modulus, v is the Poisson's ratio, Θ_0 is the Bragg angle of the material free of stress. By irradiating the sample with varied ψ angle X-ray, different Bragg angle 2Θ will be generated and the slope of linear curve plot with 2Θ versus $\sin^2\psi$ multiple by the stress constant can yield to the stress value of the sample. The peak shift profile and the linear relationship of 2Θ versus $\sin^2\psi$ is shown in Figure 1.3 below [17].

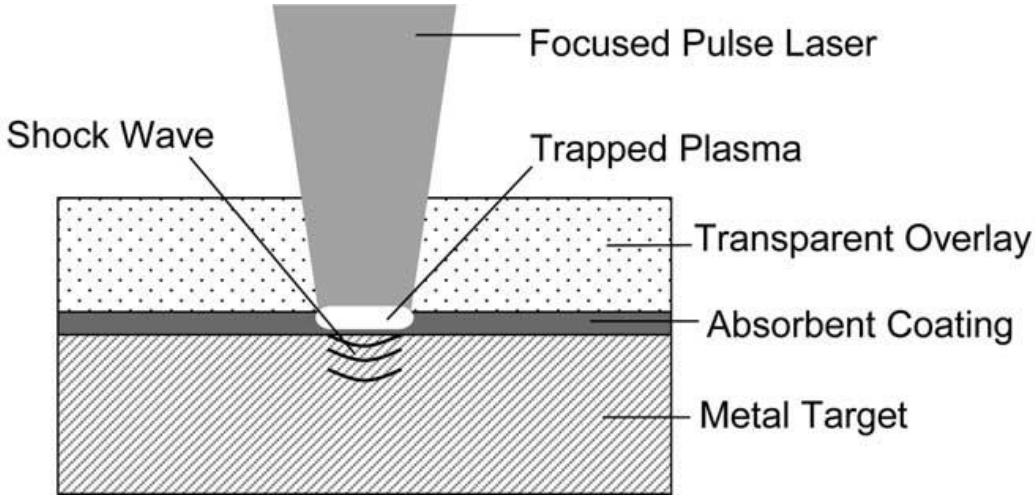

Figure 1.2 A simplified principle of the laser shock peening processing [3]

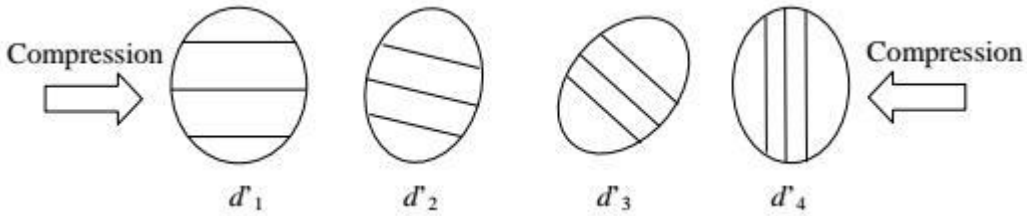

Figure 1.3(a) Effect of compressive stress on the spacing between crystal planes [17]

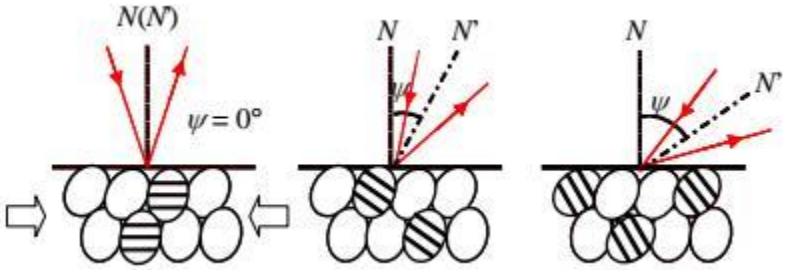

Figure 1.3 (b) Generation of psi angle due to residual stress [17]

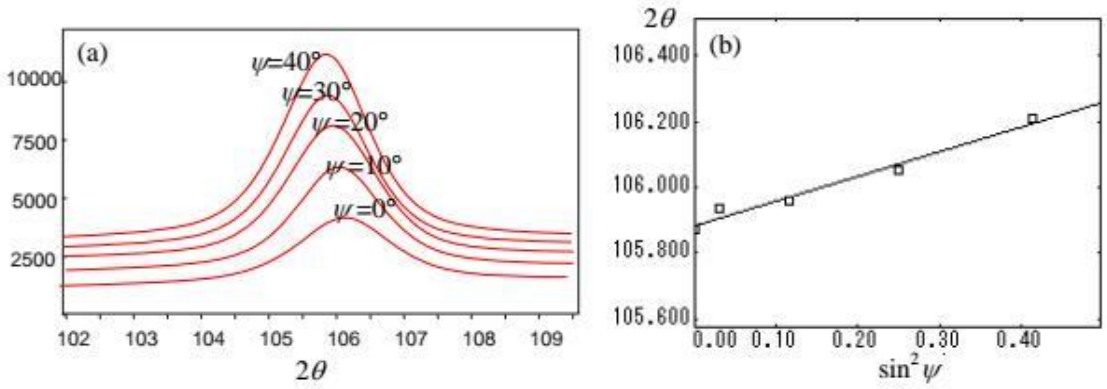

Figure 1.4 (a) Shift of Bragg angle because of the psi angle. (b) The linear relationship of Bragg's angle and sinodual psi square function [14]

There have been many experimental measurements on different laser peened alloys showing that residual compressive stress maximizes on the surface and gradually decays along the depth direction, which can be as large as over 1 mm. Figure 1.4 below shows a stress-depth profile of the AISI 304 stainless steel before and after laser shock peening as an example[18]. There are many factors that can influence the induced compressive residual stress including protective layers, laser beam parameters, peening times etc.

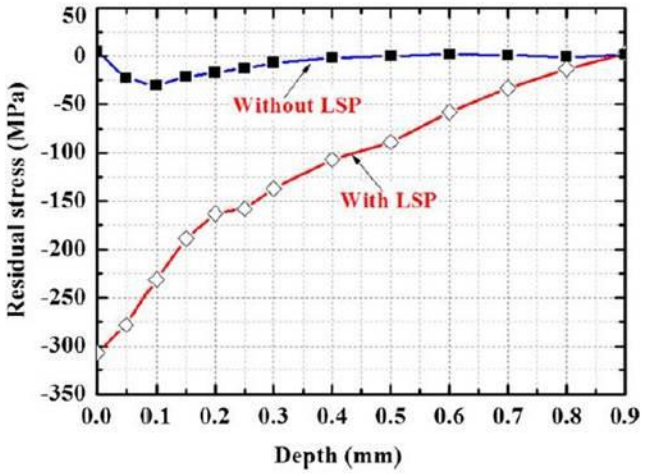

Figure 1.5 Comparison of the stress profile for the untreated and laser-peened AISI 304 steel [18].

The protective layers (coating), both the transparent overlay and the sacrificial layer serve the function of preventing the ablation and melting of the material so that laser energy can efficient generate shock wave and induce compressive residual stress. There have been studies carried out to compare laser shock peening effect on samples with and without protective layers. It was found that laser peened samples without any coating exhibited a very small amount of compressive stress, some of which even exhibited tensile residual stress [19,20] while samples with protective layers coated prior to the peening process exhibit large compressive stress. Further experiments show non-coating laser peened samples have very rough surface finish, which is a sign of ablation and will result in a high susceptibility to corrosion cracking and low fatigue life. The influence of laser beam parameters is mainly based on the fact that the laser generated shock wave is directly related to the power density of the laser beam. Consequently, the peening times matter significantly as in theory, the more peening processing have the sample went through, the larger plastic deformation and more shock wave will accumulate in the interior of the sample until saturation point is reached. Both experiment and simulation by finite element analysis demonstrate that multiple laser shots can introduce larger amount of compressive stress on surface as well as in depth[17,22]. For example, a three pulse laser peening of the 7075 aluminum alloy can lead to a largest 340 MPa compressive on the surface compared with a 240 MPa stress induced by two-time peening and a 170 MPa stress induced by one-time peening.[23] In the meantime, a three-time laser peening of 0.55% carbon steel shows a largest affected depth of 1.8 mm,

compared with a 1.4 mm affected depth for a two-time peening sample and a 0.9 mm affected depth of a one-time peening sample.[24]

1.3.3 Laser Shock Peening Effect on Mechanical Properties

Another significant effect of laser shock processing is its improvement of mechanical properties of material especially in fatigue life, toughness and hardness. Explanations for these enhancements mainly focus on the induced compressive stress both on surface and in depth and the microstructural evolution especially the generation of defects and grain refinement phenomenon.

There have been studies in many types of metallic material including steels, titanium alloys and aluminum alloys on the growth of their pre-existing crack under cyclic working showing that after subjected to single or multiple laser shock peening, samples exhibit a greater resistance against crack initiation and a slower crack growth rate [25-27]. For example, Figure 1.6 below compares the fatigue behavior of the 7075-T7351 aluminum with laser shock peening, shock peening and without any surface treatment [28]. It shows the sample can endure the largest numbers of work cycle after laser peening while sample without any surface treatment has the shortest fatigue life. The reason it that both crack initiation and crack growth requires tensile stress, by inducing compress residual stress, they can serve as a barrier against this fatigue behavior and thus increase the fatigue life and fatigue strength. Note Figure 1.5 also shows that shot peening is able to produce similar effect but less profound as laser shot peening does.

This accounts for the fact that shot peening leads to a very rough surface finish – the uneven pits are favorable sites for crack initiation and development. As a result, the effect of induced compress stress was attenuated.

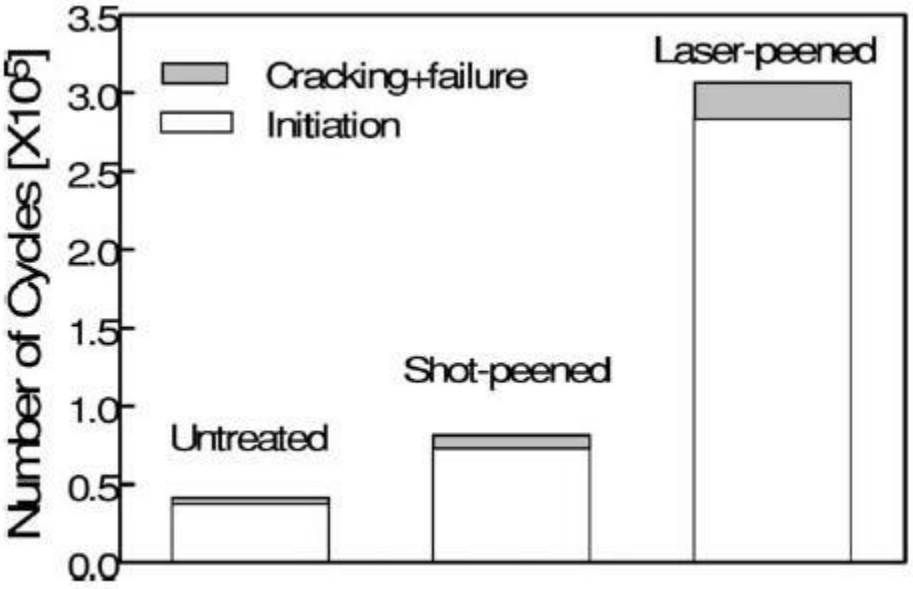

Figure 1.6 Comparison of fatigue behavior for 2024-T3 aluminum alloy samples subjected to no treatment, shot-peening and laser peened [28].

Some of the researchers perform hardness tests on laser shock peened metals including aluminum alloys and different grades of steels. They found that the increase of hardness is highly related to the peening times, laser parameters and the microstructure of the original materials. For instance, A.Clauer el at. discovered the hardness of 304 stainless steel displays a large increase from 250 Khm to 430 Khm, which is about two times with the increasing number of peening times, as Figure 1.7 shows[29]. In contrast, G. Banas el at. performed laser shock peening on two types of aluminum alloys and their hardness increase only around 10%, Figure 1.8[30]. The most possible reason for this difference in

hardness is due to different microstructural evolution. As for aluminum alloys, laser shock peening can generate simple two-dimensional defects, of which dislocation is the most common type. For steel samples, however, in addition to dislocations and stacking faults, recent reports from J.Z Lu found that laser shock peening can lead to grain refinement on ANSI 304 stainless and AISI 8620 steels [31,32]. They also proposed a grain refinement mechanism of ANSI 304 steel which is achieved by generating mechanical twin boundaries along different directions and the intersection of those twin boundaries subdivide a large grain from originally micron level into small grains ranging from 50 nm to 200 nm grain size. The mechanism can be simplified as Figure 1.9[32].

Laser shock peening was also carried out on ceramic materials. A recent study on Si_3N_4 shows that laser peening can increase its bending strength despite producing large surface roughness [33]. Further X-ray diffraction experiment confirms this enhancement is due to the introducing of plastic strain and compressive residual stress.

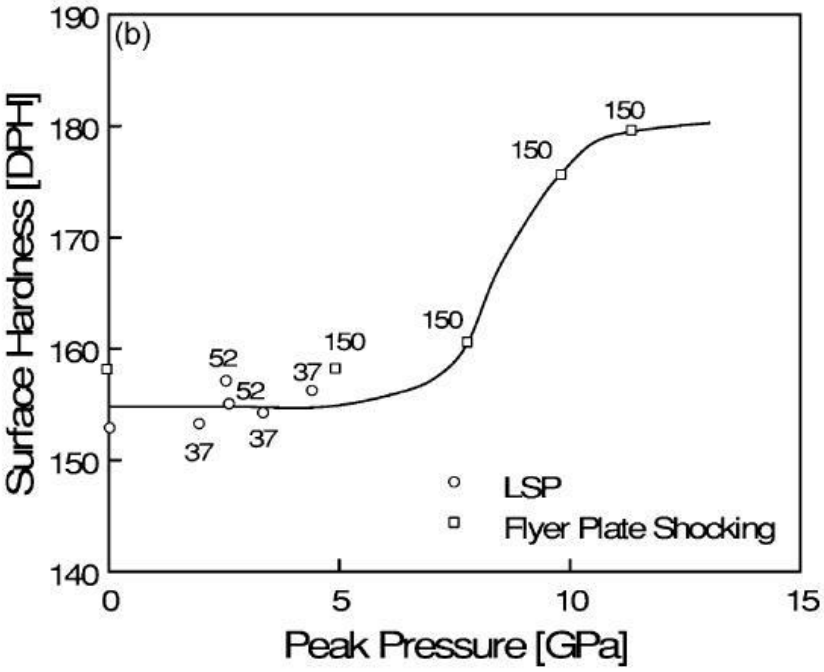

Figure 1.7 Comparison of the laser shock peening effect and flyer plate shock effect for the 2024-T351 aluminum alloy in terms of the dependence of average surface hardness on peak shock pressure[29].

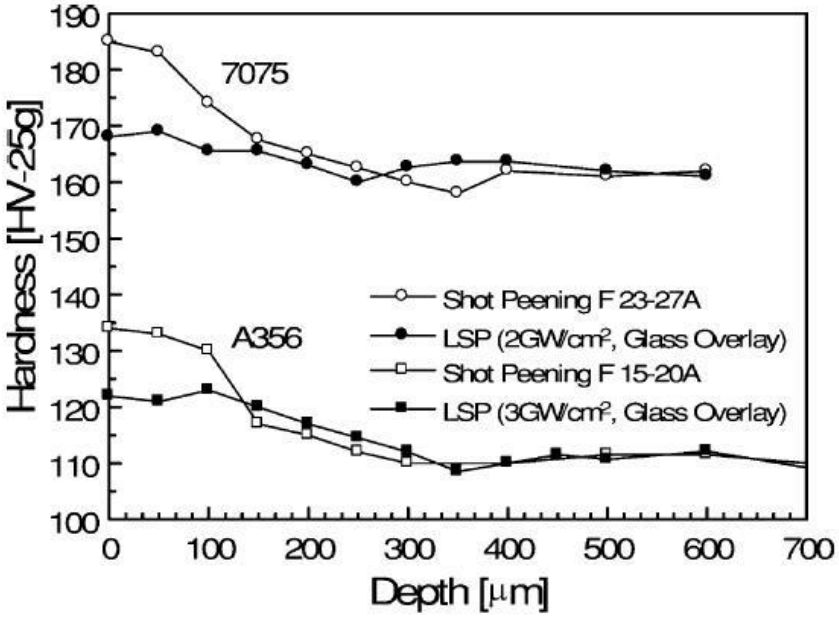

Figure 1.8 Comparison of laser shock peening and shock peening effect on Vickers Hardness for A356-T6 and 7075-T351 aluminum alloys [30]

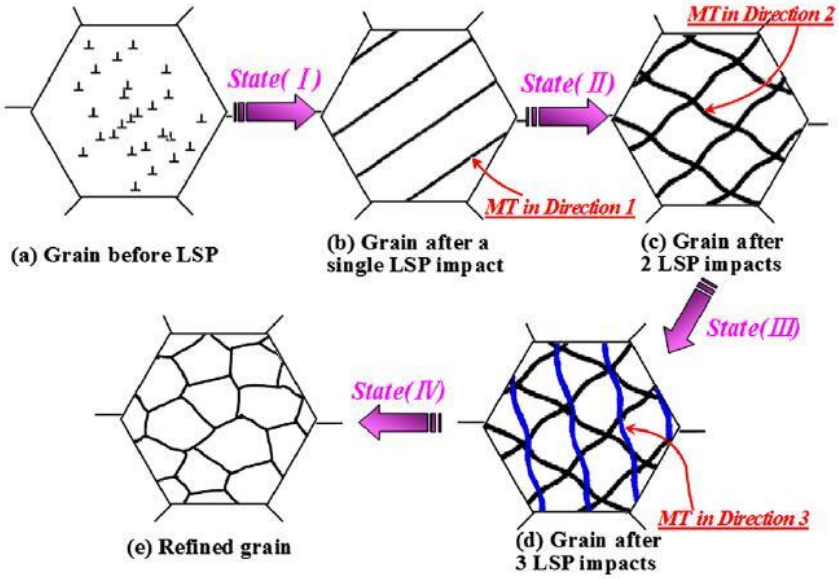

Figure 1.9 Schematic illustration on the microstructural evolution of the surface layer of ANSI 304 stainless steel subjected to multiple laser shock peening [32].

1.4 Radiation Damage

1.4.1 Influencing factors in radiation damage

Currently, 304 stainless steels along with other types of austenitic stainless steels are commonly used as cladding materials in nuclear power plant. However, the duration or the life expectancy of these austenitic stainless steels is highly limited due to the damage caused by neutron irradiation. There have been many studies on radiation damage on austenitic stainless steel and three common types of radiation defects were found: point defects (vacancy and interstitial), microscopic defects(faulted dislocation loops, cavities, radiation-induced segregation) and macroscopic changes (void swelling and embrittlement) depending on different irradiation conditions.

Generally speaking, radiance damage in austenitic steels relates to many factors including temperature, radiation dose, types of irradiation ions and transmutant gas. To quantify the radiation dose, dpa or displacement per atom was defined – dpa is the number of times that an atom is displaced under a given radiation fluence. Therefore, a material subjected to 0.1 dpa radiation damage means 10% of the atoms have been displaced from their lattice sites.

Temperature effect on radiance damage is phenomenal. As for austenitic stainless steel three temperature regime can be categorized. The low temperature regime ranges from 50℃ to 300 ℃, common radiation defects in austenitic steel include point defect clusters and dislocation loops. The mobility of these defects is limited and the density of dislocation loops will increase with the increasing temperature as displayed in Figure 1.10. The

microscopic defects including radiation-induced segregation, cavities are generally not observed until the material reaches the intermediate temperature regime from 300℃ to 700℃. In the intermediate regime, the point defect cluster and dislocation loop become thermally unstable, their density were observed to decrease rapidly with the increasing temperature, as shown in Figure 1.10. In the high temperature regime (T>700℃ for austenitic steel), all the radiation-induce defect clusters are highly mobile and thermally unstable – Dislocation loops, voids are generally annealed or annihilated. Exception is the helium (He) bubble and the He embrittlement effect where He atoms can migrate to grain boundaries with the assist of stress and cause the embrittlement [33-44].

In contrast to temperature, the dose effect on radiation damage appears much more straightforward – the larger irradiation dose (longer irradiation time), more severe the radiance damage will occur. Here, more severe damage refers to the increase of defect density. It should be also noted that migration and thermal stability of radiation defects, point defect clusters and dislocation loop in particular, can be affected by dose effect. For example, at very high irradiation dose, annealing of vacancy clusters which are supposed to take place in the high temperature regime, can occur at intermediate temperature [38].

In the meantime, the type of irradiation ion can also make significant difference. For example, S.J. Zinkle [39] reported that helium irradiation produced a higher density of cavities (i.e. severer radiation damage) than hydrogen irradiation in the same irradiation condition for many types of metals and ceramics. Other studies in heavy ion irradiation (Kr^{+}, alpha-iron, Ni^{7+}, Ag^{9+} etc.) indicate faster and more drastic damage will occur than the light ion irradiation given the same temperature and total dose [46-48].

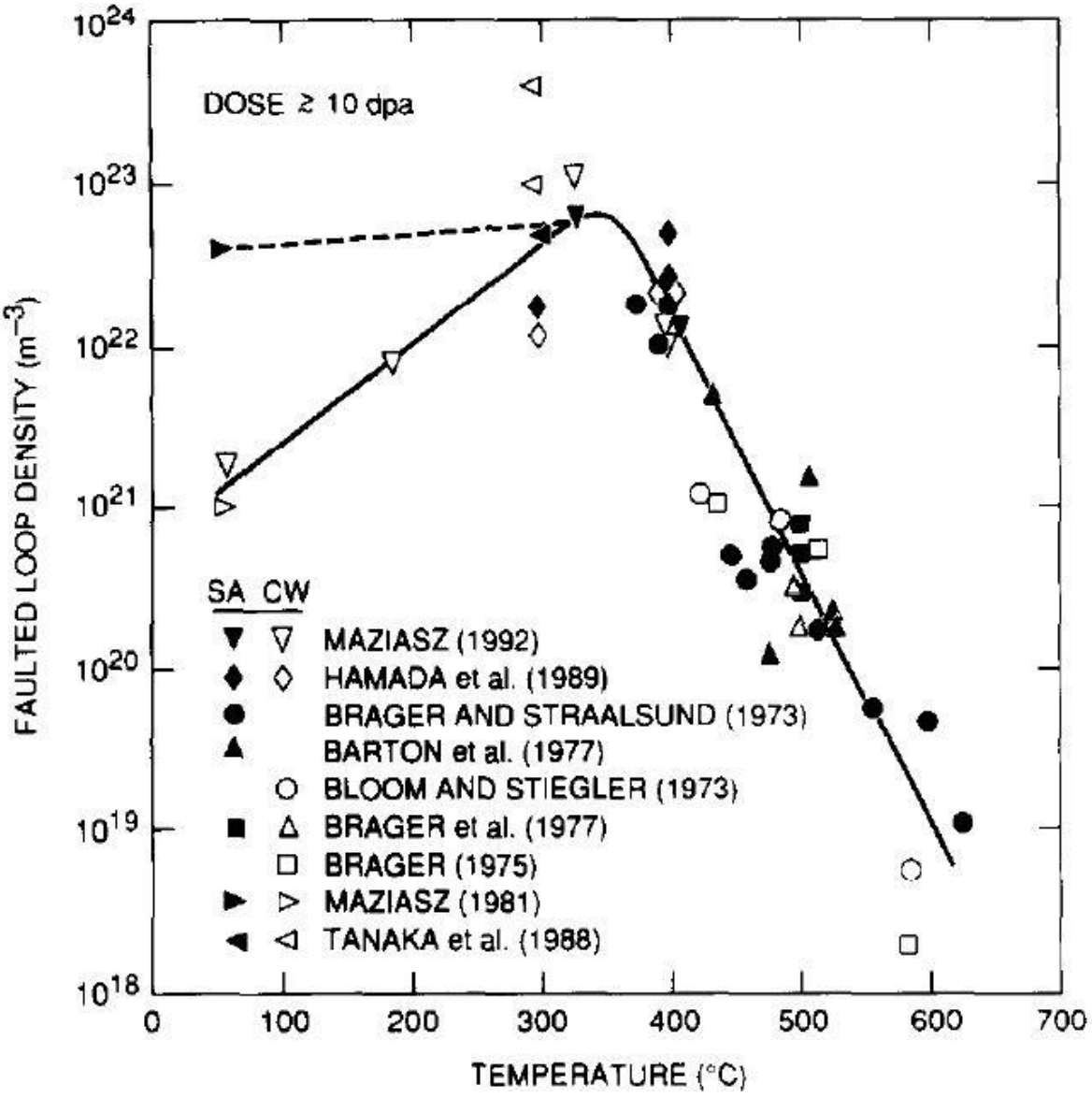

Figure 1.10 Temperature effect on faulted dislocation loop density of different types of austenitic stainless steel under neutron irradiation [38].

1.4.2 Enhancement of Radiation Resistance

There have been many approaches proposed and tested to enhance the radiation resistance in the past five decades. Generally speaking, they can be divided into two

categories: developing inherently high radiation tolerant materials and introducing stable high-strength sinks [38,48].

Among the great varieties of newly developed materials, oxide-dispersion-strengthened (ODS) alloys are one of the most promising structural materials for the new generation nuclear power plant. They are known as material with excellent mechanical properties (high strength, creep resistance at high temperature) and radiation resistance, which all originate from introducing the nano-sized oxide particles. For example, nano-sized yttrium oxide can act strong obstacles to slow down or hinder the dislocation motion, thus increasing the stress threshold for plastic deformation. In the meantime, these oxide particles are highly stable at high temperature (T can be as high as1627K), they can prevent the diffusion of atoms along grain boundaries, thus resisting the creep behavior. Finally, oxide particles can also act as sinks to absorb defects generated by irradiation, which gives ODS alloys a high radiation tolerance. Many studies on ODS alloys have confirms the existence of large numbers of oxide particles with a size approximately or less than 10 nm, which are evenly distributed in the alloy matrix by transmission electron microscopy (TEM) as well as atomic probe tomography (APT) [49-53].

Another approach to increase radiation resistance is by introducing high-strength-sinks. This approach was first proposed by modeling based on kinetic rate theory. These models predicted that by introducing high-strength sinks, for example high density dislocation or highly dispersed nano size precipitates, both point defects and large scale defects such as void swelling and radiation induced segregation would greatly alleviate[55-59]. While

the boundary between a high and a low strength sink is not clear and depends on different materials, the sink strength can be quantified based on the sink types. For instance, sink strength of cavities S_c can be determined using the following equation:

$$S_c = 4\pi r_c N_c (1 + S^{1/2} r_C) Z_c \quad \text{Eqn. 2}$$

where S is the cumulative sink strength, Z_c is a constant of unity, r_c is the radius and N_c is the density. Because grain boundaries and dislocations do not have radius, their sink strength can be simplified as:

$$S_{gb}=60/d^2 \quad \text{Eqn. 3}$$

where d is the diameter for the grain and

$$S_d = Z_d \times \rho_d \quad \text{Eqn. 4}$$

where ρ_d is the dislocation density[31]. In the case of ferritic steels, sink strength needs to reach over $10^{16}/m^2$ in order to effectively resist radiation damage. Studies have shown that at low temperature regime ($T<0.3T_m$), radiation hardening of ferritic steels will not alleviate when sink strength less than $10^{16}/m^2$. This is the same for the He embrittlement which occurs as at the high temperature regime. Yet, once sink strength increased to over $10^{16}/m^2$, radiation hardening and He embrittlement were clearly suppressed as it is observed the radiation produced point defects and radiation generated He atoms are effectively captured by these sinks. This phenomenon was summarized by S,J. Zinkle and displayed in Figure 1.11 below[35]. Some of the grain boundaries can act as high strength sinks and thus, increasing the number of grain boundaries by refining grain size is

another way to introduce high strength sinks. C.Sun el at. applied equal channel angular pressing technique and successfully prepared a ultrafine grain 304L stainless steel whose an average grain size around 100 nm. They performed Fe ion irradiation on the ultrafine grain 304L stainless steel at intermediate temperature and found the swelling resistance has increased by almost one magnitude [54].

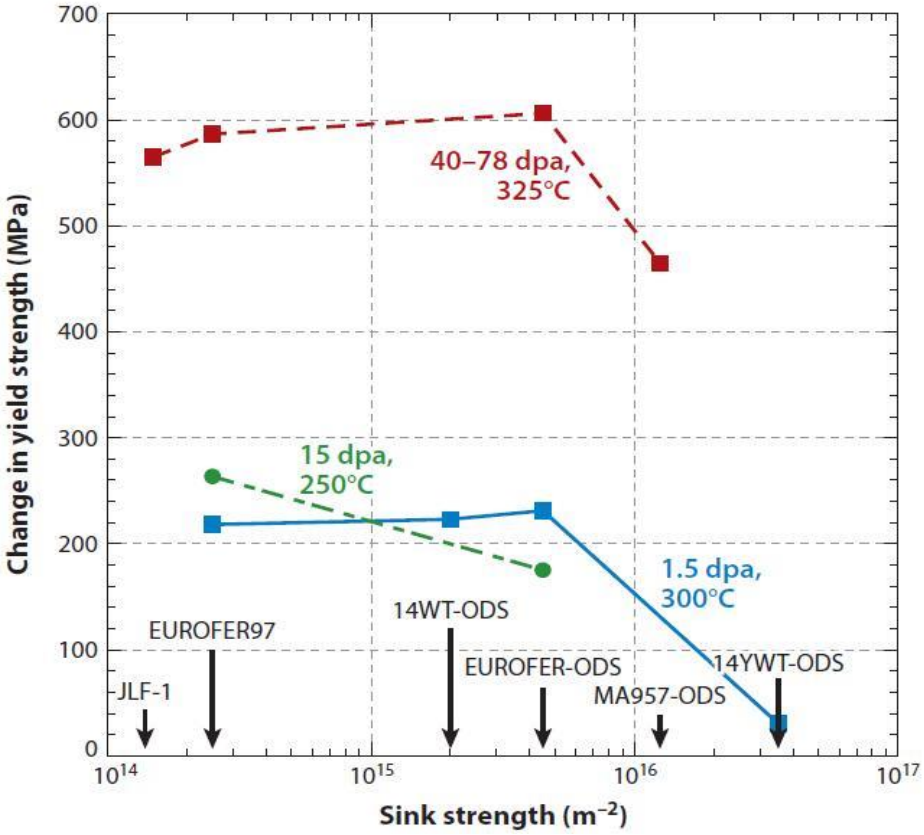

Figure 1.11 Effect of sink strength on alleviating radiation-induce hardening at different radiation dose and temperature conditions [31].

1.5 Stress Corrosion Cracking in Austenitic Stainless Steels

1.5.1 Influence Factors in Stress Corrosion Cracking

Stress corrosion cracking (SCC) is a type of environment-induce-cracking that commonly takes place in pipeline steels, austenitic steels, aluminum alloys, brass etc. and can cause severe damage or even failure of those materials. There are two main types of SCC in terms of their propagation morphology in grain structure: intergranular stress corrosion cracking (IGSCC) and transgranular stress corrosion cracking (TGSCC). For IGSCC, crack prefers to grow and propagate along grain boundary because grain boundaries become the most vulnerable sites due to the element segregation or chromium depletion. As for TGSCC, crack will propagate across the grain. The propagation direction of TGSCC is usually not random but along the crystal planes with low indices such as {100}, {110} and {210}. Figure 1.12 below shows a typical IGSCC in carbon steel and TGSCC in brass [60, 61]. In general, the occurrence of SCC requires the following three conditions simultaneously: tensile stress, corrosive environment and susceptible microstructure. Figure 1.13 below is a schematic demonstration about the required conditions for SCC [62].

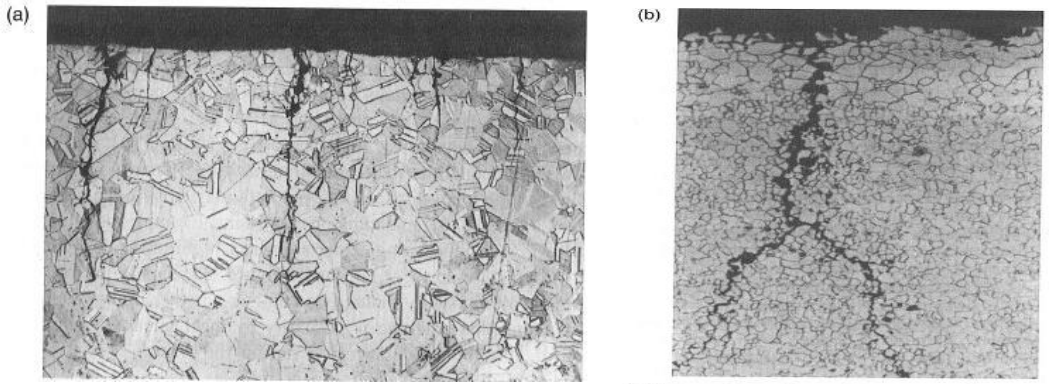

Figure 1.12 Cross-section SEM images of metallic material suffers from stress corrosion cracking: (a) TGSCC in brass. (b) IGSCC in carbon steel [60,61]

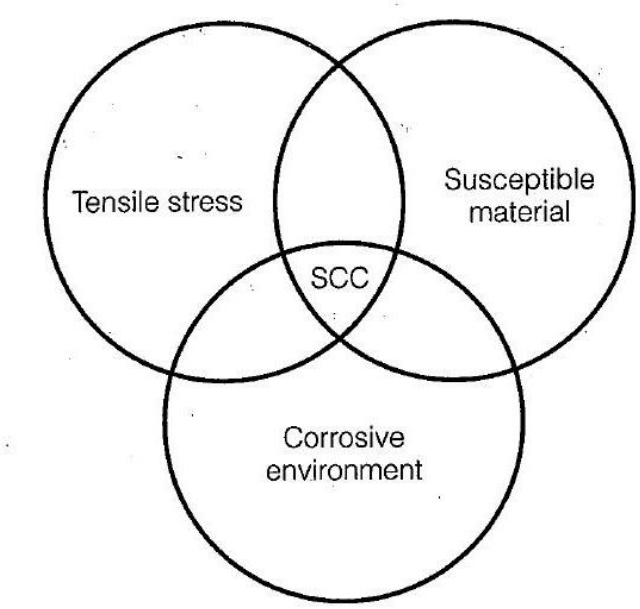

Figure 1.13 Prerequisites for stress corrosion cracking: tensile stress, susceptible microstructure and corrosion environment simultaneously [62]

Tensile stress can be either residual or applied, but it is generally a static stress with a relatively low threshold compared with other types of cracking. Although it depends on

different material system and environment, in many cases, a tensile stress in a range of 100 MPa to 200 MPa is sufficient to produce SCC.

The corrosive environment also depends on material type, temperature and pH value. For a specific material, the electrochemical potential is of great importance to the occurrence of SCC. Figure 1.13 shows the anodic polarization curve with two zones where passive films can be easily broken, making the material susceptible to SCC. In zone 1, the potential is close to the pitting potential, making pitting corrosion easy to occur and once pits are formed, passive films can be broken, which makes the material vulnerable to SCC. The austenitic stainless steel in the hot $MgCl_2$ solution is an example for zone 1-SCC. In zone 2, although the potential is far lower than pitting potential, it just passes through the transition from active region to passive region. As a result, the passive film in zone 1 is unstable and is easy to be ruptured. In theory, the increase of acid concentration (decrease of pH value) and temperature will narrow the passive region and make corrosion easier to take place. In practice, however, the situation is much more complicated as the pH value is not an independent factor, instead it correlates the existence of other polluted ions and the corrosion mechanism of a specific material system. For example, the effect of pH value is particularly significant in SCC of pipeline steels. Here, high pH value environment usually refers to the bicarbonate (HCO_3^-) or carbonate-bicarbonate solutions (CO_3^{2-} +HCO_3^-), whose pH value is around 9.0. The high pH value environment along with tensile stress can cause IGSCC in pipeline steels. In the meantime, low pH value environment usually refers to a dilute aqueous solution with a pH value around 6.5. The crack morphology in this case is usually transgranular with a

large lateral width [63-66]. The involvement of chloride ion is also important or in many cases detrimental to almost all the material regarding to corrosion. Seawater is one typical source for chloride or chloride ions which can come from salt such as sodium chloride, magnesium chloride, calcium chloride etc. The effect of chlorides is that it can reduce the potential range for passive region and make the passive film unstable [58]. Consequently, corrosion can easily take place with the presence of chloride and once a material is subjected to corrosion damage such as pits, breakdown of the passive films, crack can be easily initiated.

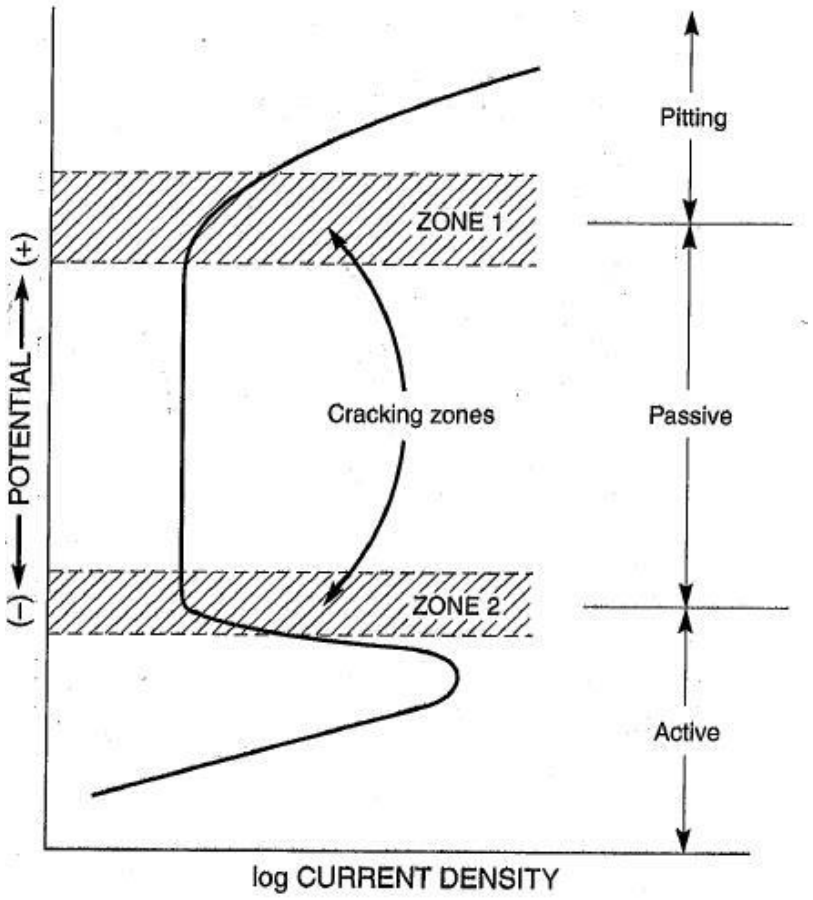

Figure 1.13 Anodic polarization curve showing two zones susceptible to SCC [58].

A susceptible microstructure means a crystal structure where SCC can easily initiate and propagate. It depends on the composition, sensitization temperature, orientation of the stress etc. For instance, austenite or FCC structure is one common of SCC susceptible structure in stainless steel while ferrite or steel with BCC structure has a relatively high SCC resistance compared with austenite. All those variations mentioned above relate to the SCC mechanisms, which will be introduced below.

To describe the SCC process, one method is to determine the relationship of crack growth rate as a function of stress intensity factor. SCC crack growth rate is denoted as dN/da, which can be determined from the relationship of curve length and time. Stress intensity factor K is defined in fracture mechanics to describe the stress state of a crack tip. There are three modes of cracking loading, as shown in Figure 1.14 and SCC satisfies mode I (K_I). In addition, the expression of K_I depends on the system and stress state – in this experiment, we use the model 'Edge crack in a plate under uniaxial stress' shown in Figure 1.15 and the K_I is given by the following equation:

$$K_I = \sigma\sqrt{\pi a}\left[\frac{1+3\frac{a}{b}}{2\sqrt{\pi\frac{a}{b}}(1-\frac{a}{b})^{3/2}}\right] \qquad \text{Eqn. 5}$$

where all the geometrical parameters a, b are shown in Figure 1.16, б is applied stress or stress at the crack tip. The theoretical relationship of crack growth rate and K_I is displayed in Figure 1.16 [63] and the SCC crack growth can be divided into three stages accordingly. Stage I is where the crack initiates and starts to propagate, its growth rate

increase exponentially. When SCC comes to stage II, a steady state is reached – crack will grow in a constant rate with the increasing stress intensity factor and but when it enters stage III, crack will grow in an exponential rate until the material fails [64].

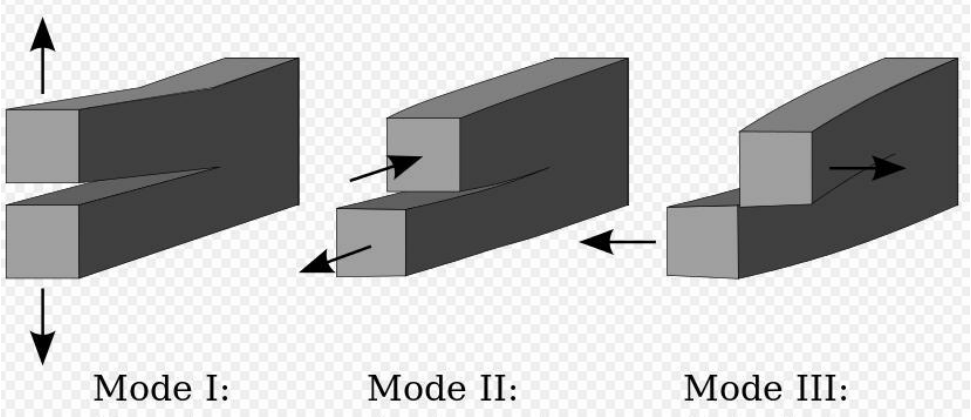

Figure 1.14 Three cracking mode in fracture mechanics. In Mode I, crack is generated by tensile load. In Mode II crack is generated by in-plane shear and for Mode III also known as tearing mode, crack surface will move in an opposite direction. Image is in courtesy of 'D.P Rooke and D.J. Cartwright', Compendium of stress intensity factors [63].

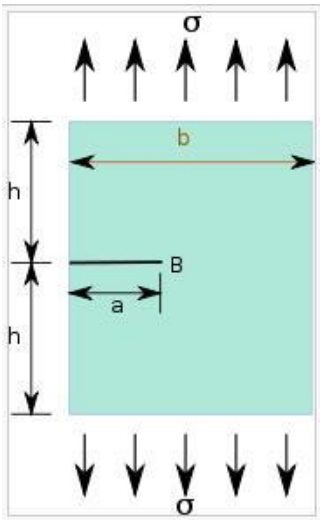

Figure 1.15 'Edge crack in a plate under uniaxial stress model' for determining K_I, where a is the crack length, b is the material length, h is the width [63].

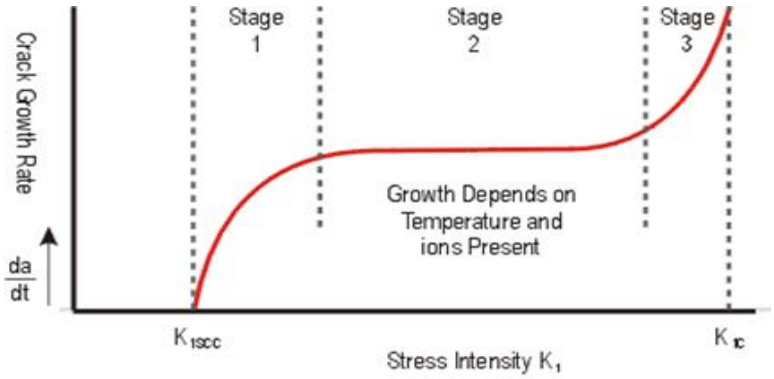

Figure 1.16 Theoretical curve of crack growth rate as a function of stress intensity factor K_I [64].

1.4.2 Proposed Mechanism for Stress Corrosion Cracking

There have been many studies in modeling and experiments trying to explain the mechanism of SCC. Thanks to their work, there are more than six SCC mechanism proposed [62], three of which will be reviewed in this part, including the film rupture model, hydrogen-induced SCC and film-induced cleavage.

The film rupture model is a classic model. It states that crack is firstly initiated because the accumulated strain produced by the tensile stress ruptured the protective passive film on the surface. After that, crack will grow by anodic dissolution in which the electrochemical reaction occurs and the material will dissolve in the anode. With cracks propagate, the material will eventually fail in a relatively short amount of time. The process of film rupture can be schematic shown in Figure 1.17. Further research on SCC experiments confirm that crack initiation is by breaking down of the protective film, however, debates are in the mechanisms on crack propagation[64]. For film rupture model, electrochemical process is proposed to be the dominant way for crack propagation.

Another SCC mechanism that has been widely studied and discussed is the hydrogen-induced SCC (HISCC). The principle of HISCC is that hydrogen atoms can diffuse to the interior of the material and contaminate the material either by weakening the atomic bonds or by the formation of hydrides. This contamination can facilitate the crack initiation or crack growth, i.e. embrittle the material. The extent of embrittlement is highly related to hydrogen concentration. There is a study on low-alloy steel showing that the crack growth rate rises with the increase of hydrogen concentration and it is around two magnitudes higher than the growth rate without hydrogen contamination, as Figure 1.18 shows. Because hydrogen has a preferential diffusion path to grain boundary and interface, HISCC is generally intergranular [64]. In other words, the HISCC proposed that crack propagation is governed by hydrogen embrittlement.

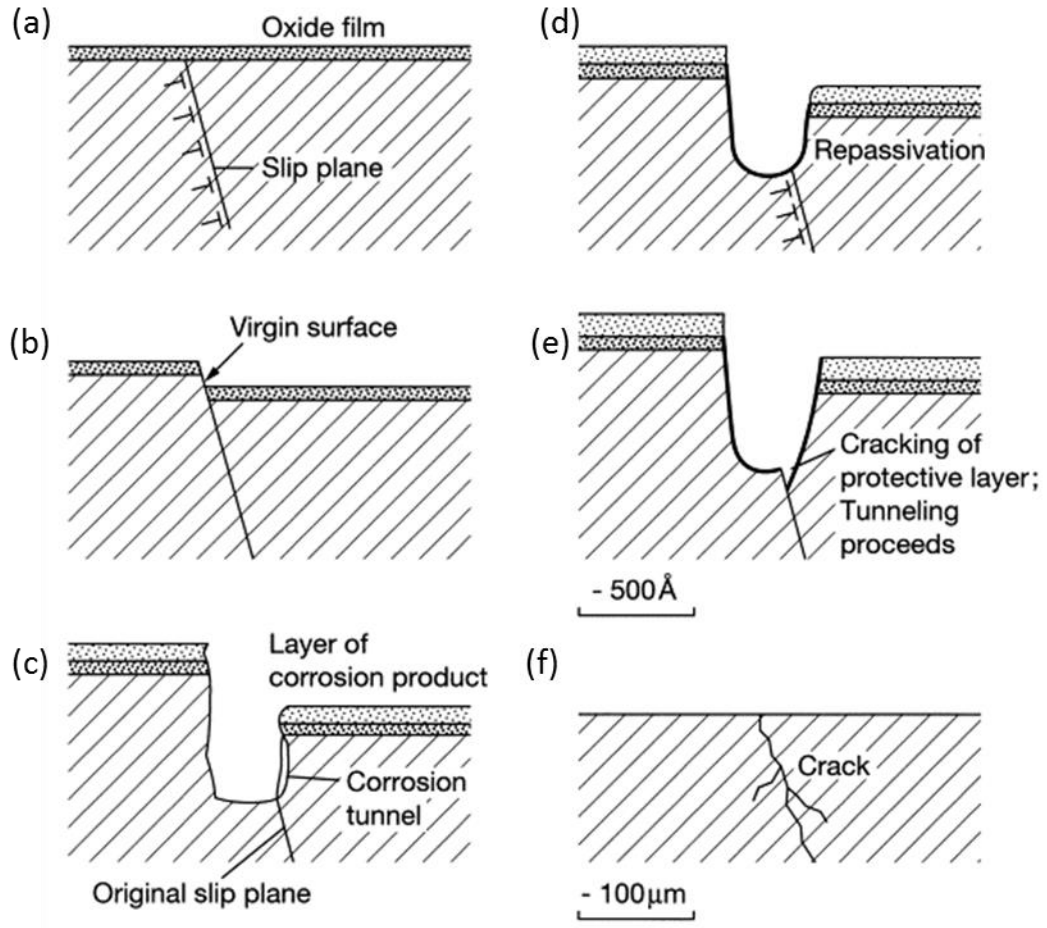

Figure 1.17 Illustration of the film rupture model. SCC starts from (a) where gliding of slip planes occur along the depth direction and makes the unfilm material exposed to the corrosion as (b) shows. With the stress corrosion takes place, the passive film will be broken as (c) shows. In this case, repassivation may occur and a passive film can be formed again, shown in (d). However, because of the stress or strain, gliding of the slip planes can occur again (e) and crack will propagate as (f) shows [64].

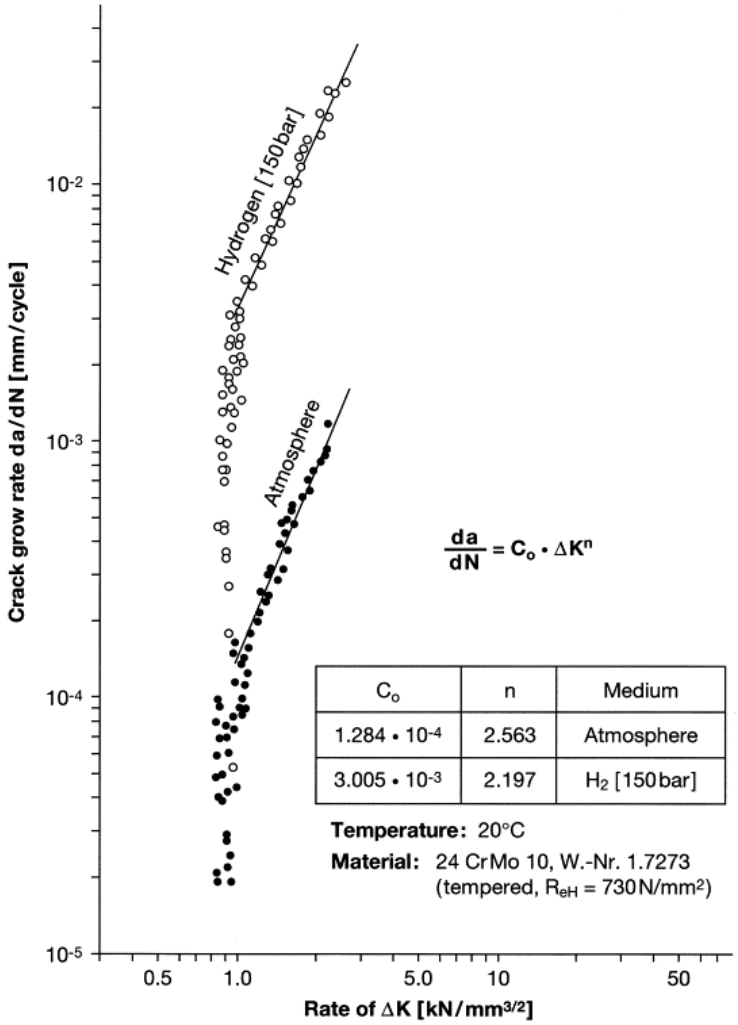

Figure 1.18 The effect of hydrogen contamination and hydrogen concentration on growth rate of SCC in a low alloy steel [64].

Film-induced cleavage (FIC) is of significance for SCC in stainless steels. It proposes that crack propagation is mainly because of a high concentration of stress or strain in the crack tip. In other words, the FIC model emphasizes that cracks grow in a mechanical process and thus, a relatively rough and brittle fracture surface is resulted. The morphology of the cracks grow with this mechanism are transgranular cracks in most cases.

CHAPTER 2: EXPERIMENTAL METHODS

2.1 Sample Preparation and Laser Shock Peening Treatment

The composition of as-received bulk steel samples (304 stainless steel and 304 ODS steel) is listed in Table 1. The samples were first cut by a diamond saw into 10 mm ×8 mm × 2 mm rectangular solids. Then their surface was mechanically polishing with silicon carbide grinding paper in a roughness range from #240 to #1200, followed by polishing with alumina power in an order of 3 μm, 1 μm and 0.3 μm. After ultrasonic cleaning with acetone and ethanol, laser shock peening was carried out. The utilized laser source is known as Q-switched Nd:YAG. The pulse energy was 850 mJ and the duration time was 7 ns. Prior to LSP, the samples were coated with a 177 micron thick black tapes on the surface as sacrificial layers to avoid ablation and flowing water was used as confining layer. All the steel samples would undergo the same LSP process five times, with a 50% overlap of the area and for each time of LSP, the black tape was replaced. The detailed parameters of the LSP process are listed in Table 2 and the basic equipment as well as the simplified LSP process can be displayed in Figure 2.1 and Figure 2.2 respectively.

Table.1: Composition of Austenitic Stainless Steels

304 stainless steel:

Composition	Fe	Cr	Ni	Mn	Si	P	C
Percent (wt%)	Bal.	18.3	8.5	1.38	0.06	0.03	0.04

304 ODS steel:

Composition	Fe	Cr	Ni	Mn	Si	Ti	Y_2O_3
Percent (wt%)	Bal.	18.2	8.2	1.20	0.06	0.7	0.35

Table 2: Laser Shock Peening Parameters

Type	Value
Spot Size (mm)	1
Pulse energy (mJ)	850
Duration time (ns)	7
Overlap	50%
Repetition-rate (Hz)	10
Laser wavelength (nm)	1064
Beam profile	Gaussian
Laser Pulse	5

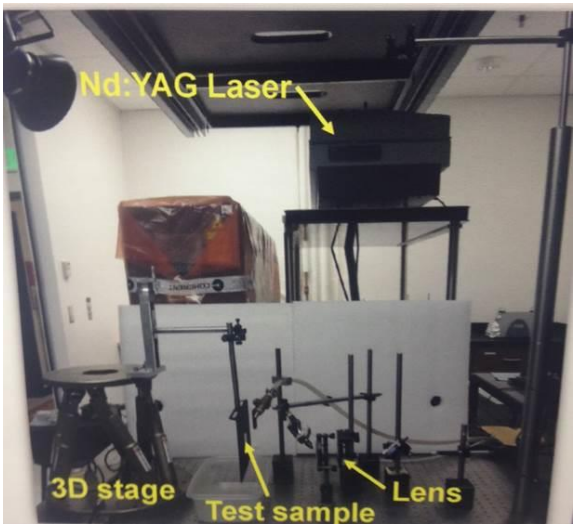

Figure 2.1: In the courtesy of Dr. Dawei Li in Prof. Yongfeng Lu's group.

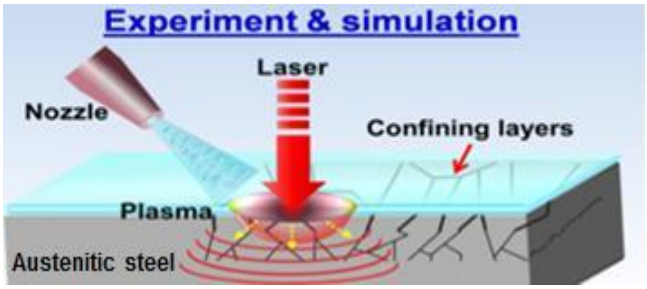

Figure 2.2: In the courtesy of Dr. Dawei Li in Prof. Yongfeng Lu's group

2.2 Microstructure Characterization of the LSP samples

After the steel samples were laser peened, the grain structure of the cross-section of the laser-peened samples was studied by SEM. The cross-sectional areas were obtained by cutting the LSP sample with a diamond saw, followed by mechanical polishing and ultrasonic cleaning. In order to clearly observe the grain structure, chemical etching was carried out prior to the SEM imaging. The etching solution for 304 stainless steels are 3:2:2 volume ratio of HCl:HNO_3:acetic acid plus several drops of glycerin and etching solution for 304 ODS steels are 2:1:7 volume ratio of HF:HNO_3: H_2O. For comparison, the cross-sections of the untreated samples were also etched and observed by SEM.

To obtain a deeper insight in LSP effect on microstructure of the austenitic steel, TEM characterization was used. To prepare the TEM samples, the LSP steels were firstly thinned to less than 200 micron by mechanical polishing and punched into 3-mm diameter discs followed by further polished to a thickness less than 100 micron. Final thinning was achieved by twin-jet-polishing. Twin-jet-polishing, also called electro-polishing is a thinning method based on chemical corrosion. According to Faraday's law:

$$r = \frac{i_0 a}{nF} \quad \text{Eqn. 7}$$

where a and n are constant for a specific system and F is the Faraday's constant. From Eqn. 7, the material remove rate r is proportional to the current density i_0. Figure 2.3 shows the ideal current density curve from the instructional manual of Struers Inc[67]. As is shown, in the segment AB, the sample will undergo etching due to the direct anodic dissolution, which will ends up uneven and coarse surface finish, making the sample unable to be observed in TEM. Segment CD is the best area for making a good TEM sample as the current density remains constant, i.e. the material is removed in a constant rate, which can produce an even and thin finish. After that (in segment DE), the sample will be subjected to oxidation, which will eventually lead to the formation of pits and oxide layer. As a result, the two key steps of twin-jet-polish is to obtain a calibration curve similar as Figure 2.3 shows [67] and to select an appropriate voltage/current density to ensure the material remove rate in a moderate and constant speed. For 304 stainless steels, one of the most commonly used electrolytes is 5% perchloric acid + 95% methanol at -20℃. A calibration curve with a wide CD segment can be obtained, from 13.5V to 17.0V. In this experiment, a voltage of 14.5V was chosen. After final thinning by twin-jet-polishing, the steel samples could have their thickness decreased to less than 100 nm and became electron transparent.

To quantitatively analyze the LSP effect on the microstructures of the austenitic steel samples, the twin density and the dislocation density were calculated. From the cross-sectional SEM images of the LSP and the untreated samples, the twin density was determined by the number of twin boundaries in a specific region divided by the area of

that region. Then an average value was obtained by analyzing all the data from over thirty different regions. Similarly, the average dislocation density was determined for LSP and untreated samples using the same statistical method except that TEM images instead of SEM images were used.

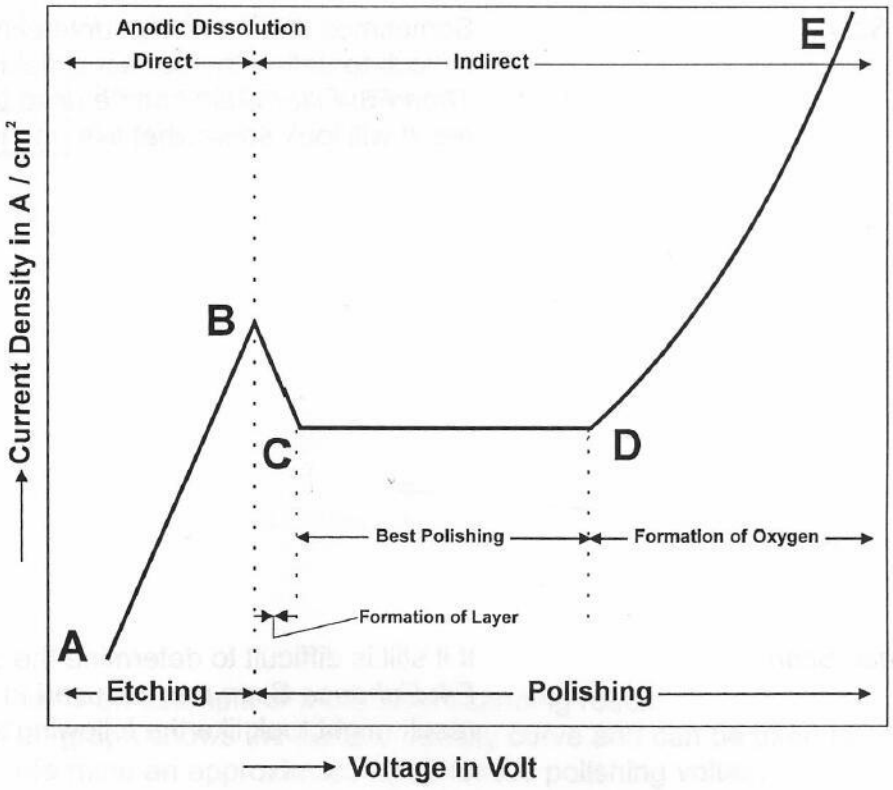

Figure 2.3 In the courtesy of the Struer Company: Calibration curve of the twin-jet-polishing, described by the voltage as a function of current density [67]

2.3 In-situ irradiation TEM experiment for LSP and untreated samples

To investigate the behavior of the LSP steel samples under irradiation, in-situ TEM irradiation experiments were carried out by the intermediate voltage electron microscope (IVEM) equipped with an accelerator at the Argonne National Lab. The TEM samples

were firstly observed by TEM to identify regions with large amount of defects such as high density dislocations or dislocation walls, twin boundaries and stacking faults. To obtain a good resolution with high contrast of above defects in TEM, high diffraction contrast is needed. Diffraction contrast is a form of amplitude contrast in TEM which is based on the scattering of crystal lattice at Bragg's angle. Since austenitic stainless steels are crystalline materials and their crystal structure are face-center cubic, there are many diffracted beams generated along with one incident beam. Here, we achieved a high diffraction contrast by enabling the two-beam condition: when the sample was tilted certain angle to a condition where that only the incident beam and one strong diffracted beam past through, two-beam condition is achieved. By blocking the other diffracted beams and thus minimizing the their interference, two beam condition gives a very high contrast and consequently, many two-dimensional defects including dislocations, twins, stacking faults as well as point defect clusters can be observed in TEM.

The irradiation condition was carefully selected to simulate the nuclear power plant environment and to investigate the LSP effect on the radiation induced point defects. The voltage used for irradiation was 1 MeV and the dose started from 0 to 1.33 dpa. Two temperature conditions were used: room temperature and 300℃. According to the Chapter 1 and S.J Zinkle's report [38], stainless steel is in the low temperature regime at room temperature and at 300℃. Therefore, most radiation defects will be dislocation loops.

To observe the behavior of dislocation loops with increasing dose and at different temperature, dark field imaging is needed. Bright field and dark field are two basic TEM

modes for amplitude-contrast imaging. The principle is shown in Figure 2.5[68]: Basically, bright field is generated by moving the objective aperture to let incident beam form the image while dark field is to let the diffracted beam form the image. As a result, bright field imaging gives a very high magnitude illumination, but the low contrast limits its ability to observe the small scale radiation defects. Dark field imaging on the other hand, gives a very high contrast and enables the observation of dislocation loop or other point defect clusters produced by irradiation.

To quantify the accumulation of radiation damage in the austenitic steel samples, loop density as a function of dose was determined. The term 'loop' in this case refers to all defects caused by radiation at low temperature regime, including vacancy clusters, interstitial clusters and dislocation loop. There are two general expressions of loop density: the number of loops per unit area or the number of loops per unit volume. In this experiment, thickness of the TEM samples can be ignored and thus, loop density is determined as the total number of loops divided by the total area of the region. In the measurement of total number of loops, sometimes it is difficult to identify or confirm a specific loop because of the low illumination in dark field imaging. In that case, all these loops are counted as one half, as suggested by Z. Yao el at[69]. Meanwhile, to minimizing the error, an average loop density was determined using a similar statistical method as the determination of the dislocation density and twin density. The error bars in all those calculation are the standard deviation.

Figure 2.4 IVEM (with an accelerator) for the in-situ irradiation TEM experiment at the Argonne National Lab.

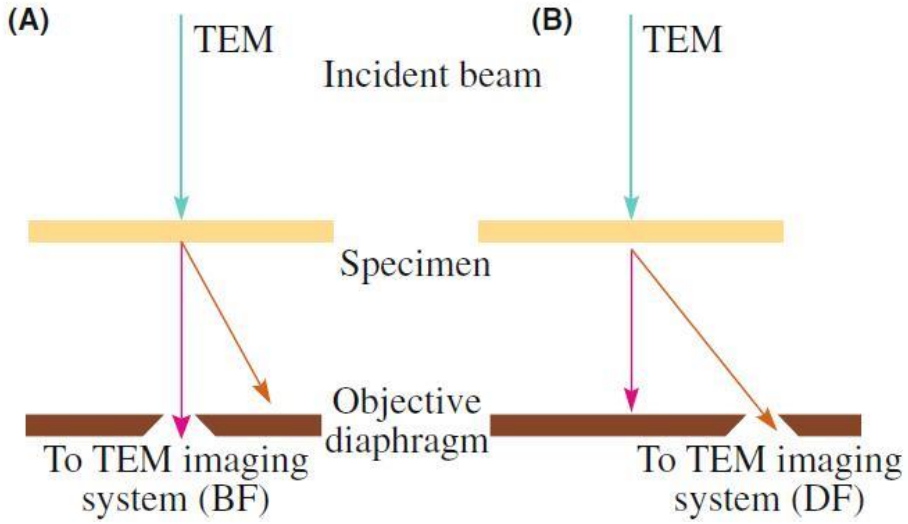

Figure 2.5 Schematic illustration of the bright-field and dark-field mode in TEM imaging [68]

2.4 Stress Corrosion Cracking Tests for LSP and untreated samples

The untreated and LSP austenitic steels samples were subjected to a SCC environment with applied tensile stress in order to study the LSP effect on the SCC of the austenitic steels. The equipment for stress corrosion cracking test is called Proof Ring System from Cortest. The setup is shown in Figure 2.5. Precision machining is needed for the preparation of the SCC samples and they were carried out in the machine shop at the Nebraska Center for Material and Nanoscience at University of Nebraska Lincoln. The dimension of SCC sample is displayed below in Figure 2.6. The test area is the central part of the sample with a length of 1.015 ± 0.15 inches and the LSP was performed on this part. After subjected to LSP, the steel samples were put into the vessel and immersed into the solution. Temperature control can be achieved by connecting the system to a temperature monitor provided by Cortest. The key point of this test is to apply a constant tensile stress. To achieve that, a constant load is required, which is generated by producing displacement of the ring. By tightening the screw on top of the ring and measuring ring deflection with a venial caliper, the applied load can be determined with the aid of the calibration curve shown in Figure 2.7 below. The measurement process can be simplified by the following equations[70]:

$$\text{Displacement d} = \text{initial ring distance } D_i - \text{final ring distance D} \quad \text{Eqn. 8}$$

$$d = 8.409E^{-13} * load^3 + 1.2161E^{-9} * load^2 + 9.6628E^{-4} * load - 1.092E^{02} \quad \text{Eqn. 9}$$

$$\text{Tensile Stress } б = \text{Applied load / Sample Area} \quad \text{Eqn. 10}$$

After SCC test, the samples were put in the FEI Helios 660 FIB/SEM facility, which can accommodate the whole SCC sample and achieve surface and cross-section imaging. The cross-section of the SCC sample was obtained by cutting out the test part and machined along the depth direction, followed by chemical etching. To compare the LSP effect, this SCC test was performed on untreated and LSP of 304 stainless steels. Their cross-sectional grain structure after subjected to SCC was presented as SEM images.

To quantitatively describe the SCC behavior of our steel samples, the crack growth rate as a function of stress intensity factor was obtained. Similar SCC samples were used. However, for each of the SCC sample, a 1mm depth notch was machined at the center prior to the test. The notched samples have an advantage of a shorter crack initiation time. Because of the notch, the applied stress will concentrate on the notch site and cracks would initiate and propagate along it. After a crack was initiated, the time was recorded and the SCC sample was put into the Helios 660 to measure the crack length in SEM mode. Then the sample was moved back into the proof ring system to have its crack grown. The sample would be taken out again for every 2.5 hours to measure its crack length until the sample failed. As a result, a curve of crack length as a function of test time can be obtained. From this curve, the crack growth rate can be obtained as the slope and with the ‘Edge Crack in a Finite Plane under Uniaxial Loads’ model, the stress intensity factor can be determined. Finally, the crack growth rate as a function of stress intensity factor was obtained.

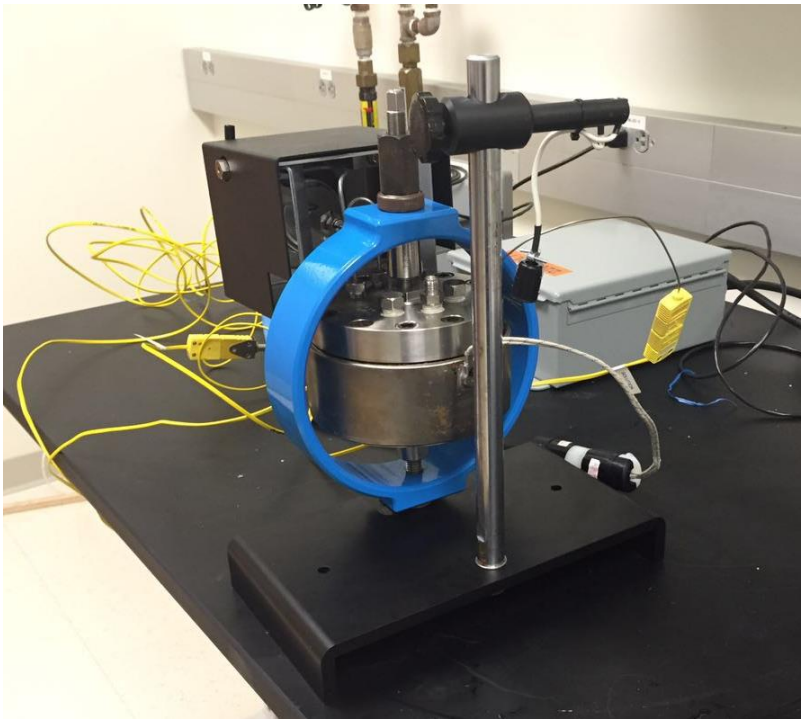

Figure 2.5: A schematic overview of the proof ring system for SCC test [70]

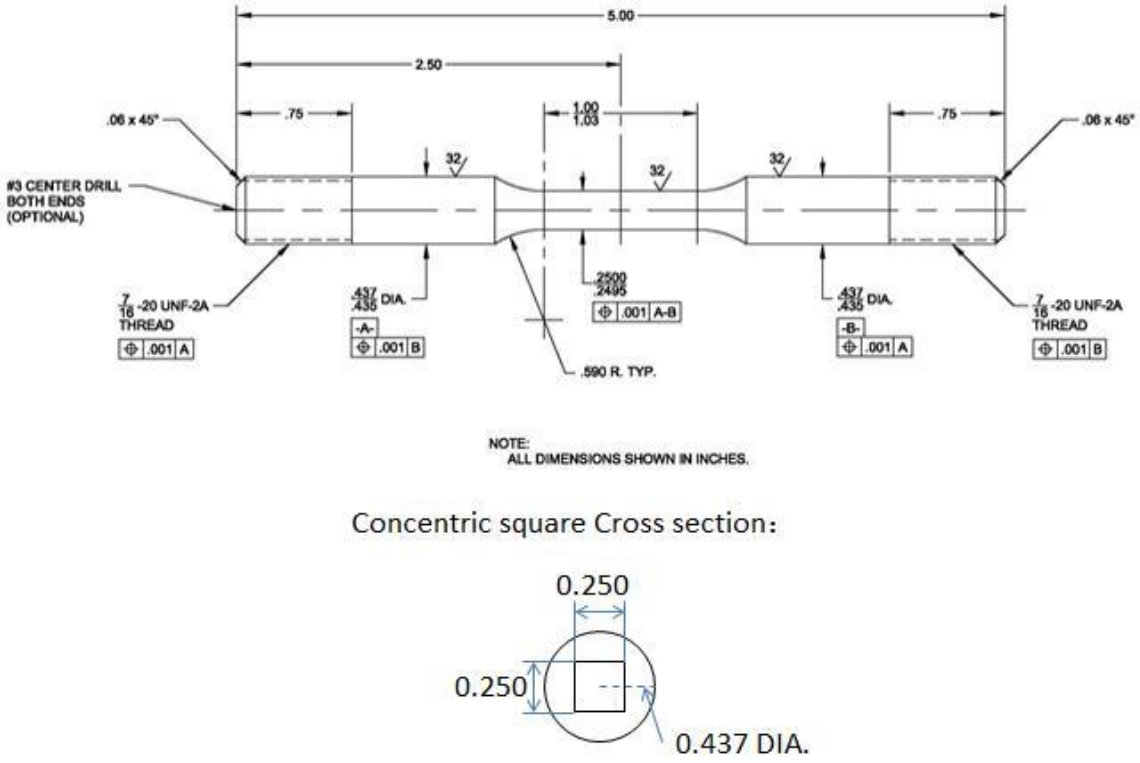

Figure 2.6: Dimension of the SCC specimen for the proof ring test system [70]

Contact: Larry Gregerson
Cortest, Inc.
38322 Apollo Parkway
WILLOUGHBY, OH 44094

TEST REPORT — EAR-CONTROLLED DATA

Date:	12/26/2014
P.O. No.:	28271-SK
W/O No.:	COR013-14-12-09396-21
Date Received:	12/4/2014

Sample Description: One (1) Proof Ring, 3/8" Wall, Calibrate to 3400 KG, S/N: 10035, P/N: 31016-2

LOAD DEFLECTION TEST

Displacement = 8.4049E-13(LOAD)^3 + 1.2161E-09(LOAD)^2 + 9.6628E-04(LOAD) - 1.2092E-02

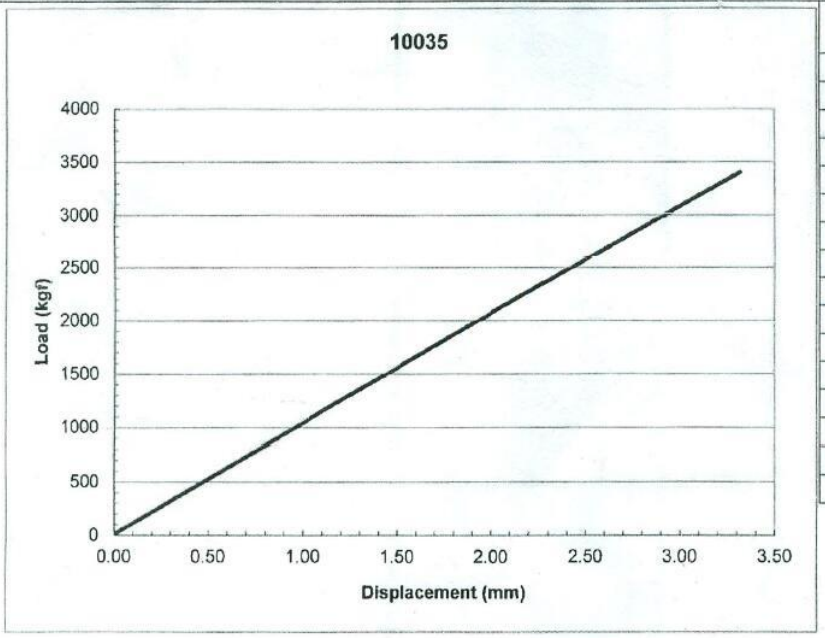

Axial Load (kgf)	Deflection (mm)
500	0.471
700	0.665
900	0.859
1100	1.053
1300	1.248
1500	1.443
1700	1.638
1900	1.834
2100	2.030
2300	2.227
2500	2.424
2700	2.622
2900	2.821
3200	3.120
3400	3.320

Figure 2.7: Calibration curve: a relationship between the displacement of proof ring and the applied load [70].

CHAPTER 3: RESULTS AND DISCUSSION

3.1 Observation of cross-sectional grain structure by SEM

The cross-section morphologies of the 304 steel samples before and after five pulses LSP are shown in Figure 3.1. As the laser peening effect is profound in the near surface region and decreases along the depth direction, SEM characterization was focused on regions close to the surface (depth is less than 1 mm). As shown in Figure 3.1 (a), after five pulses LSP, larger numbers of deformation twins appear in the grains of the steel samples, some of which are arranged in a same direction as those in region A, while others appear at different directions and intercept with each other, as those in region B. The discovery of twin boundary interception is of great significance to the grain refinement process according to J.Z. Lu's report [71].The deformation twin density of the near-surface cross-section region is determined as $(1.98 \pm 0.36) \times 10^{10}\ m^{-2}$. However, the density of deformation twins start to decline at a depth of 0.3 mm and when it goes as deeply as 1 mm from the surface, no such defects are observed. This indicates that LSP effect and induced plastic strains are minimal in the substrate. In contrast, the 304 steel samples without LSP have nearly no deformation twins inside the grains at any depth, as shown in Figure 3.1(b) and their grain structure appear exactly as the grains in the substrate of the LSP samples. Therefore, the twin density of region in Figure 3.1 (b) can be approximated as zero. The comparison of the cross-sectional grain structure shows that the LSP treatments can generate mechanical twins in 304 stainless steels.

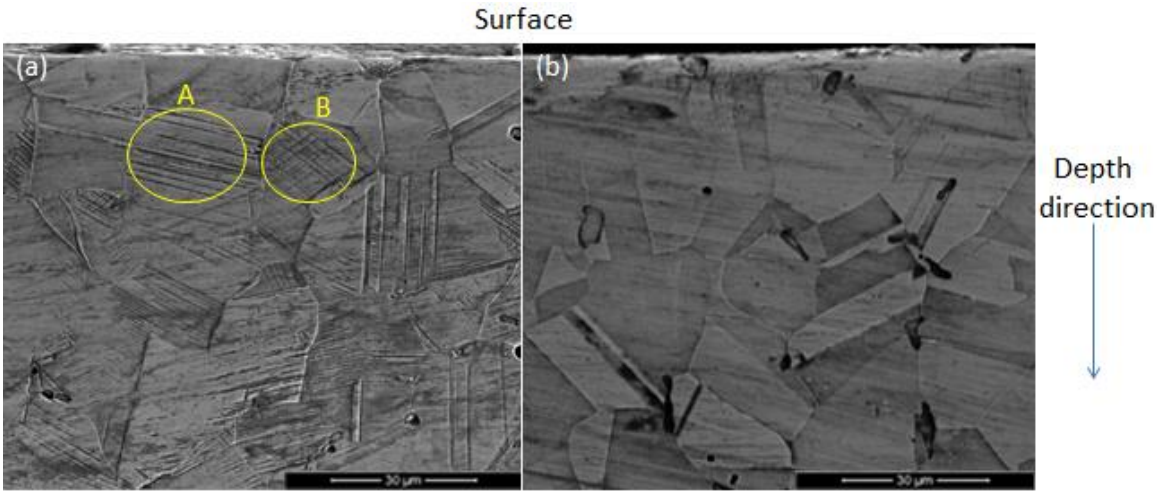

Figure 3.1 SEM images of the cross-sectional grain structure of 304 stainless steel samples subjected to: (a) 5 LSP; (b) untreated.

3.2 Observation of the surface microstructure after LSP by TEM

TEM images of the surface of the 304 steel samples after subjected to five pulses LSP are shown in Figure 3.2. The following microstructural features are identified: twin boundaries (TB), stacking faults (SFs), dislocation lines (DLs) and dislocation walls. Figure 3.2(a-b) shows the bright field and dark field images of the twin boundaries (TBs). The beam direction is [112] and **g** is (-1 -1 1). As it shows, all of the four twins are aligned along the same direction and there are dislocation lines inside the twin boundaries. The width of the TBs ranges from 33 nm to 200 nm. Figure 3.2(c-d) shows the bright field and dark field images of the high density SF region. The beam direction is [101] and **g** is (0 -2 0). It can be seen that large numbers of SFs were generated. There are also two TBs identified in this region. Figure. 3.2(e-f) shows the region with high density dislocations. The beam direction is [112] and **g** is (-1 -1 1). A large numbers of

dislocation lines and dislocation walls can be identified in that region. The average dislocation density is determined as $(9.63 \pm 1.24) \times 10^{13}$ m^{-2}.

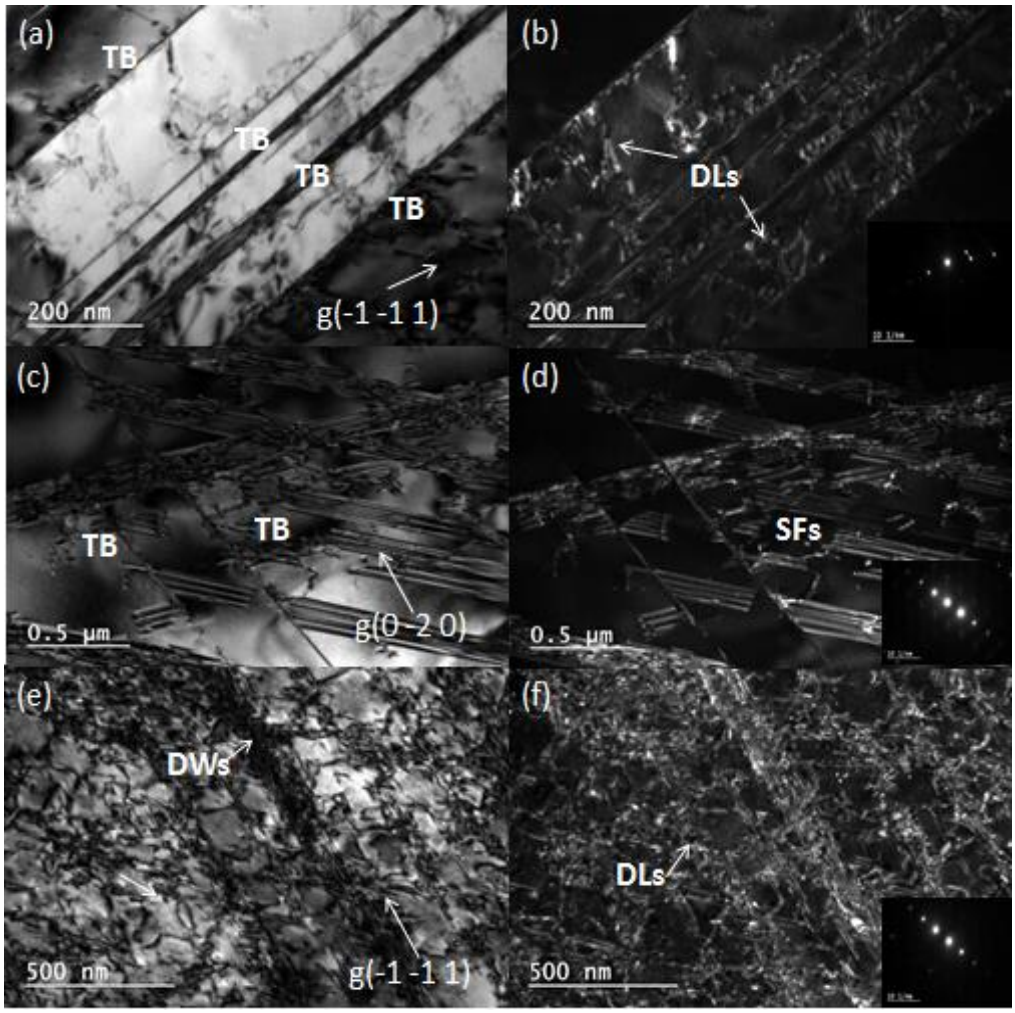

Figure 3.2 TEM images of 304 sample surface subjected to 5 LSP: (a) bright field image of the twin boundaries; (b) dark field image of the twin boundaries; (c) bright field image of the high density SFs region; (d) dark field image of the high density SFs region; (e) bright field image of the high density DLs and dislocation walls region; (f) dark field image of the high density DLs and dislocation walls region.

The TEM observation of the surface of the untreated sample was also performed. For comparison, regions with TBs and DLs are shown in Fig 3.3 (a) and Fig 3.3(b)

respectively. In Fig 3.3(a), the beam direction is [101] and **g** is (0 -2 0). The twin width is around 500 nm and the number of TBs as well as DLs are fewer than the peening sample. This TB along with a few other TBs in the untreated samples are most likely generated during preparation when the samples were subjected to the hot isostatic pressing. Although all the steel samples were annealed immediately after received, some of the TBs might remain. However, compared with the LSP samples, the number of TBs in the untreated samples is much fewer. In Fig 3.3(b), the beam direction is [112] and **g** vector is (2 -2 0). It can be seen the number of DLs is fewer than the peening surface and there is no dislocation walls found. The average dislocation density is determined as $(6.53 \pm 0.85) \times 10^{12}$ m^{-2} which is approximately an order of magnitude less than the dislocation density of the peening surface. As a result, it shows that by inducing severe plastic deformation in the form of shock waves, multiple LSP processes can not only increase the number of TBs, but can also increase the dislocation density of the 304 stainless steel.

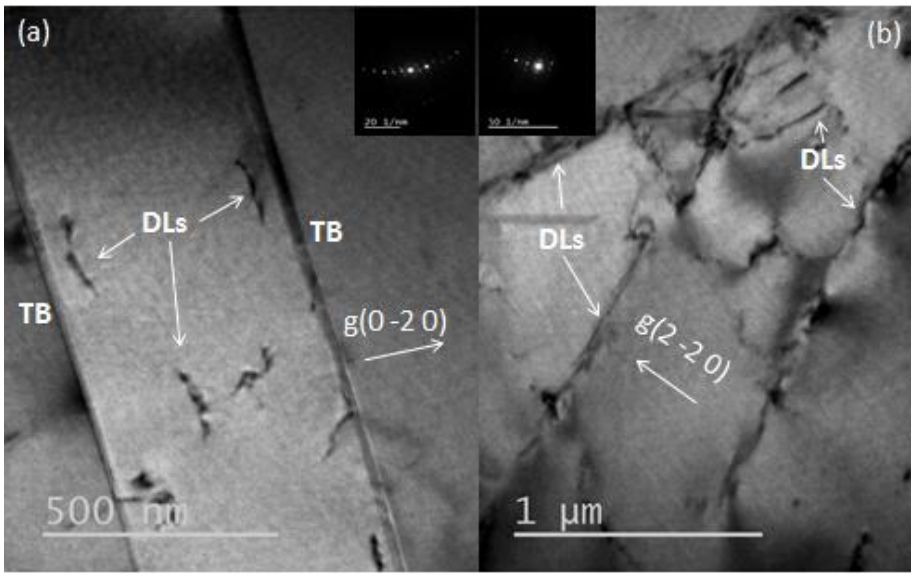

Figure 3.3 TEM images of 304 surface layer without peening effect: (a) bright field image of the twin boundaries; (b) bright field image of the DLs.

3.3 Loop density analysis at the high density dislocation region

Irradiation with heavy ion (Kr^+) on the 304 steel samples in the low temperature regime will give rise to dislocation loops, which appear as white dots in the dark field TEM mode and are considered as the dominant irradiation defect in this temperature regime. Note that at room temperature (r.t) and 300℃, interstitials are expected to dominate over vacancies. Prior to irradiation, regions with the following microstructural features were chosen: SFs, TBs and DLs with dislocation walls. When the irradiation process began, videos were recorded in those regions and the loop density at different dose condition can be obtained. Similar analysis was carried out for samples heated to 300℃, videos were also recorded in the annealing process.

Fig 3.4 shows the process of loop absorption by DLs. In Figure 3.4(a), the image can be considered at 0s when one dislocation loop moved to the DL. Then Figure 3.4(b) can be considered 6s later when the first loop was gradually absorbed and a second loop appeared. Figure 3.4(c) was 25s later when the first loop disappeared while the second loop became weaker. Finally, Figure 3.4(d) was taken 101s later when the second loop was completely adsorbed by the DL and disappeared, indicating DL's ability to act as sink as well. In fact, the high density dislocation has been confirmed as one of the effective high strength sinks for radiation defects [72, 73]. The effectiveness can be quantified as the sink strength of dislocation or S_d given by Eqn 4.

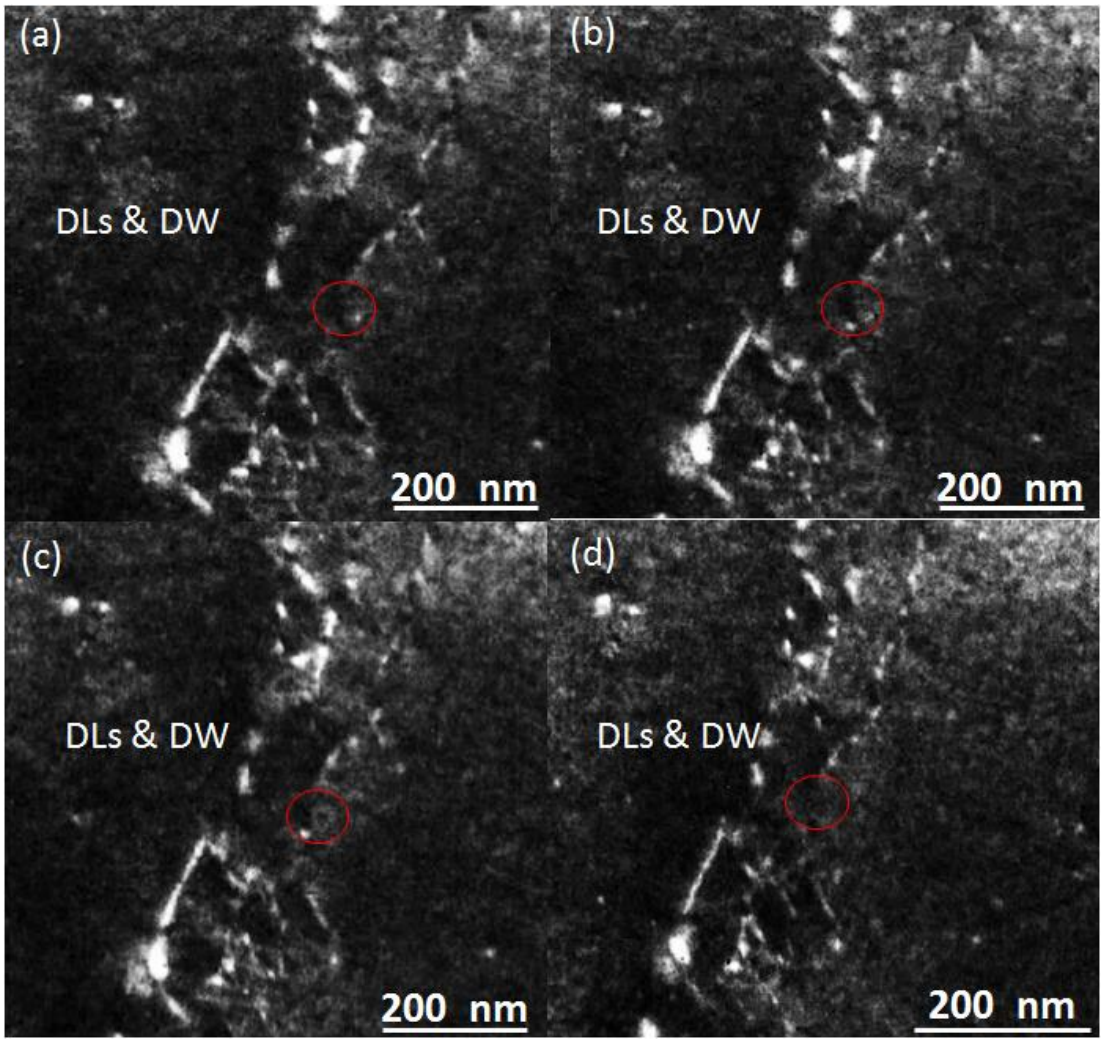

Figure 3.4 (a-d) TEM images of the 5 LSP samples in DLs and DW region in the irradiation process: (a) can be considered as 0s; (b) 6s later (c) 25s later (d) 101s later

DLs regions of the LSP 304 steel samples subjected to 0.33 dpa (1.13×10^{18} ions/ m^{-2}) and 1.0 dpa ($2.25*10^{18}$ ions/ m^{-2}) radiation dose were shown in Figure 3.5(a-b). For comparison, a region of the untreated sample with no LSP generated defects was also chosen for irradiation and the images were shown in Figure 3.5 (c-d). From those TEM images, the loop density as a function of dose for the untreated 304 steel and the LSP 304

steels can be determined and displayed in Figure 3.6. It can be seen that with the increase of dose, radiation damage becomes more severe and the loop density increases. However, the 5 LSP steel shows a much less radiation damage than the untreated steel sample. The loop density of 5 LSP steel is approximately one magnitude less than the untreated one.

The high density dislocations generated during LSP are believed to play an important role in the difference in loop density. According to Eqn.4, the sink strength of dislocation is proportional to its density for the same material. The 5 LSP sample is thus estimated to have a S_d around $(9.63 \pm 1.24) \times 10^{13}$ m^{-2}, approximately one order of magnitude larger than that of the untreated sample whose S_d is $(6.53 \pm 0.85) \times 10^{12}$ m^{-2} (as Z_d is unity). Therefore, the high density dislocations produced by the laser shock processing raised the radiation tolerance of the 304 stainless steel.

Figure 3.6 also displays a relationship of loop density vs. dose for the 5 LSP sample irradiated at 300℃. As it shows, the loop density of the 5 LSP sample after annealing is approximately 0.1 order of magnitude higher than those at room temperature (r.t) but it is still greatly less than the loop densities of the untreated sample. The slight increase of dislocation loop in the 5 LSP sample can be attributed to the temperature effect in two aspects. Firstly, increasing temperature can promote the displacement of atoms thus slightly increase the loop density, which is consistent as the pervious discovery by S.J.Zinkle in Figure 1.10. Secondly, the LSP generated dislocations became mobile upon annealing in a range (from 298K to 573K) below one third of the 304 sample's melting temperature (1723K). The video of the annealing process demonstrates this phenomenon. The velocity of dislocation motion is given by the following equation:

$$V_{dis} = f(\sigma)\exp(-E/kT) \quad \text{Eqn.11}$$

where $f(\sigma)$ is a function of stress, E is the activation energy and T is the absolute temperature [73]. The increased V_{dis} enables the glide or climb of the DLs and when two parallel DLs of opposite sign come across, annihilation will take place and this decreases dislocation density. Figure 3.7 compares the microstructure of the 5 LSP sample in a region with SFs and DLs before and after annealing at 300℃. There were five SF regions at r.t. After annealing at 300℃, only two SFs regions remained. Since SFs are formed by a high energy dislocation separated as two or more partial dislocations in low energy state, the annihilation of SFs can cause a decline of dislocation density. Given that, the average dislocation density in this region was $(9.14 \pm 1.02) \times 10^{13}$ m^{-2} before annealing, but decreased to $(6.42 \pm 0.77) \times 10^{13}$ m^{-2} after annealing and that contributes to the slight increase of radiation damage. But overall, the loop density is much less than the untreated sample.

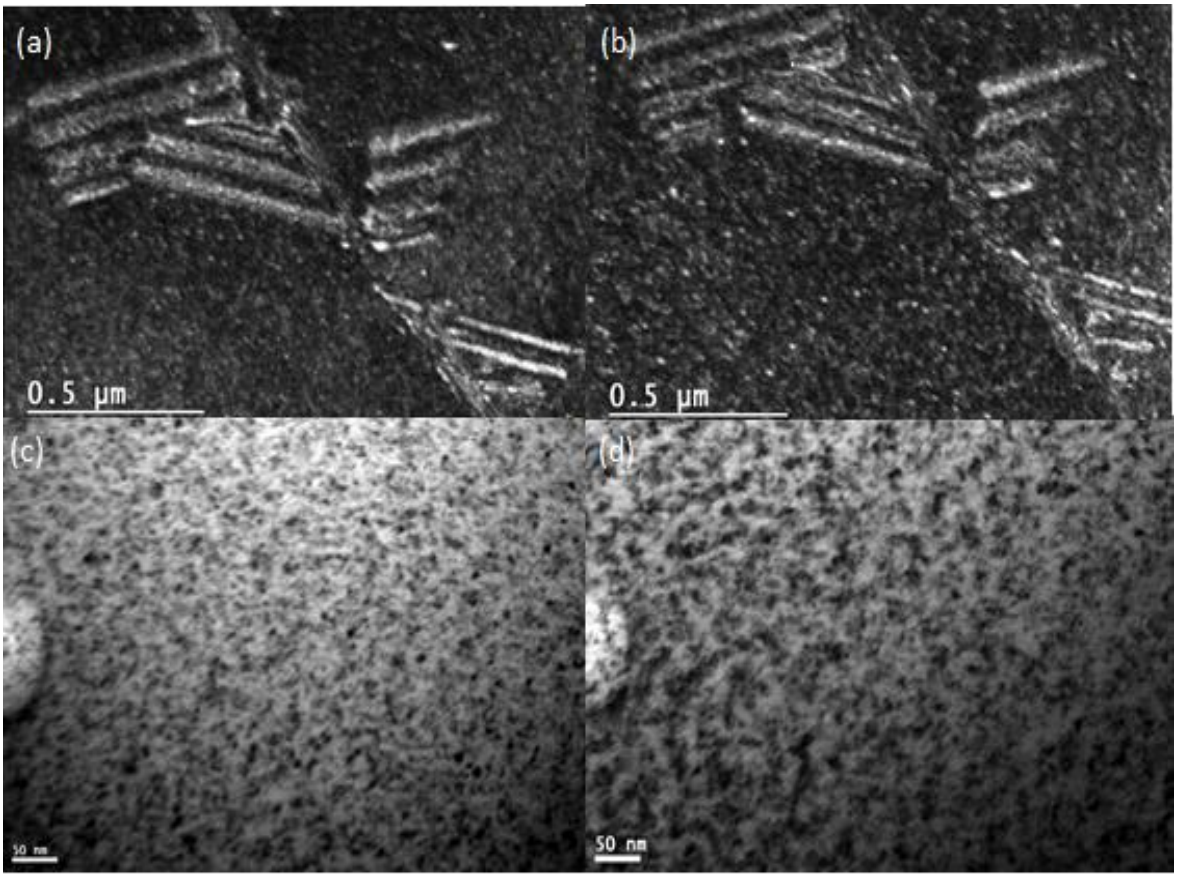

Figure 3.5 TEM images of the 5 LSP and the untreated samples subjected to different radiation dose: (a) the SFs region of the 5 LSP sample subjected to 0.33dpa; (b) the SFs region of the 5 LSP sample subjected to 1.00dpa; (c) the region without SFs or TBs of the untreated sample subjected to 0.33 dpa; (d) the region without SFs or TBs subjected to 1.33 dpa

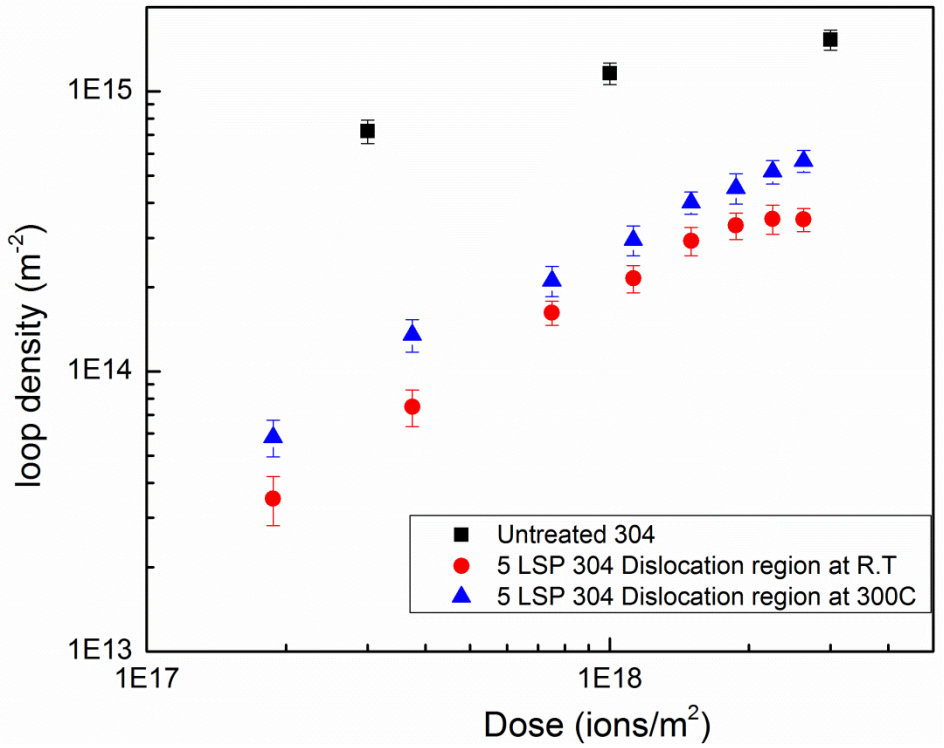

Figure 3.6 Comparison of loop density as a function of dose: untreated sample at r.t is in black rectangles; 5 LSP sample in the dislocation region at r.t is in red circles and 5 LSP sample in the dislocation region at 300℃ is in blue triangles.

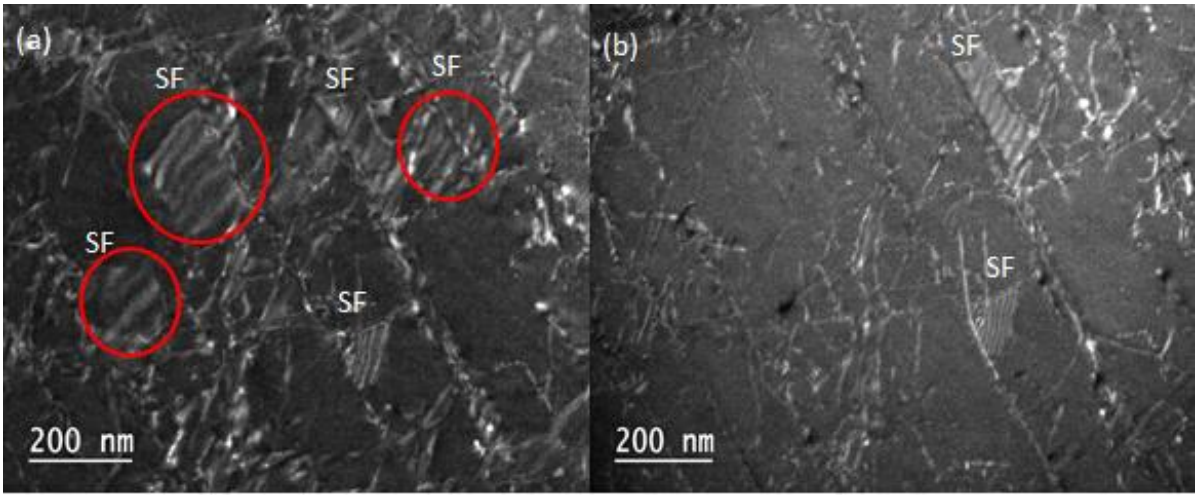

Figure 3.7 TEM images of the 5 LSP sample in the SFs region before and after annealing: (a) is at r.t; (b) is annealed to 300℃

3.4 Loop density analysis at twin boundary region

It has been reported that grain boundaries (GBs) can serve as sinks for radiation defects and that the GB sink efficiency depends on the structure, misorientation, GB plane orientation, etc. [74,75]. The sink capacity of TB, which is a special type of GB, is thus worthy of investigation. The process of loop absorption was recorded in the in-situ irradiation TEM experiment and the features of this process are displayed in Figure 3.8 (a-d). In Figure 3.8(a), a loop emerged and moved to the twin boundary. Then it became smaller and weaker in illumination as Figure 3.8(b) and Figure 3.8 (c) show. Finally in Figure 3.9(d) this dislocation loop was completely absorbed by TB and disappeared, indicating that similar as the high density dislocations, TBs can act as sinks for radiation-induced dislocation loops.

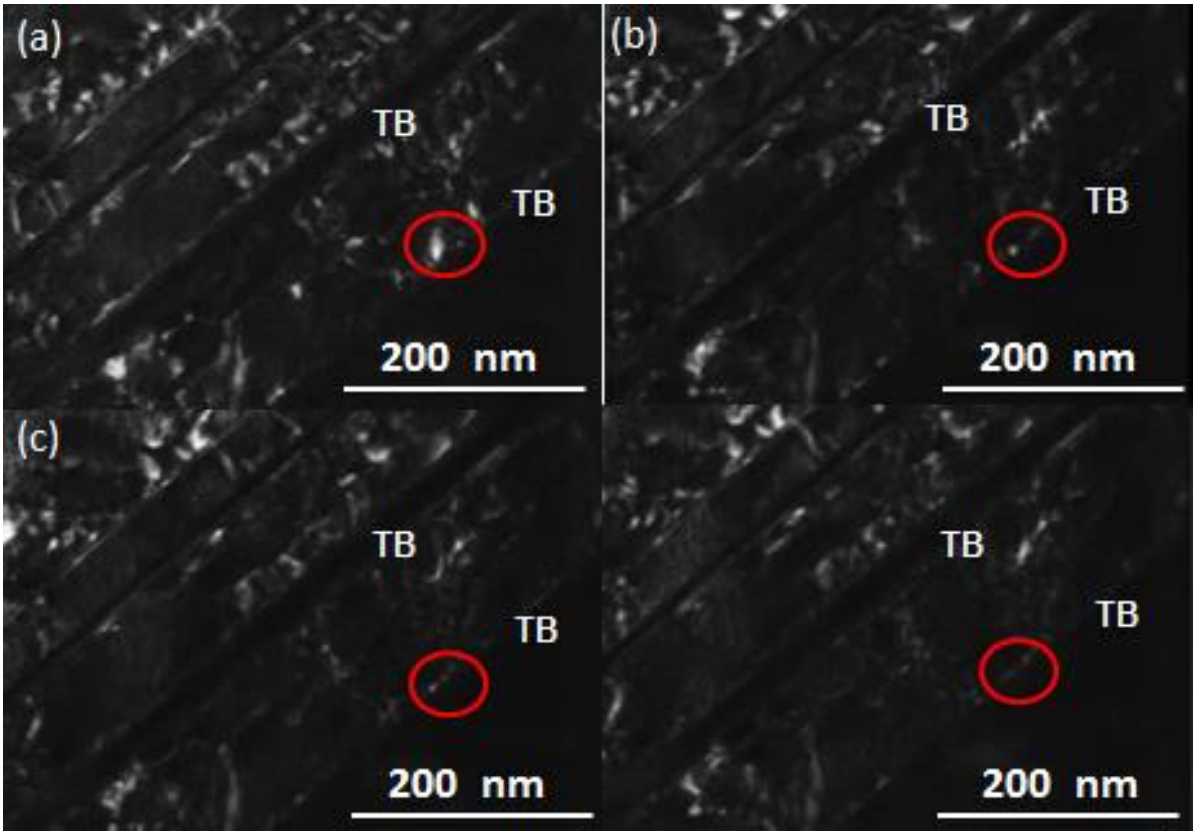

Figure 3.8 (a-d) TEM images of the 5 LSP samples in TBs region in the irradiation process: (a) can be considered as 0s; (b) 10s later then; (c) 19s later; (d) was 25s later.

A similar loop density analysis of the 5 LSP sample in the TB region at r.t was carried out and its relationship with radiation dose is shown in Figure 3.9. At r.t, the loop densities of the 5 LSP sample in the TBs region are far less than the untreated sample. In addition, they display a trend of saturation at 0.78 dpa ($1.75*10^{18}$ ions/ m^{-2}), which indicates the 5 LSP sample exhibits a higher irradiation resistance than the untreated sample because of the LSP generated TBs.

In order to investigate the effect of temperature, irradiation was also performed in the TB regions at 300℃. The corresponding loop density and dose relationship was shown in Figure 3.9 as well. In the beginning when dose is low, the annealed sample has its loop densities close to the loop density of the 5 LSP sample at r.t. With the dose increased, the loop densities slightly exceed the r.t ones. The effect of temperature on the twin boundary was observed different than the dislocations. As the annealing video shows, the TB is stable upon annealing at 300 ℃. However, as Figure 3.8 shows, there are certain numbers of dislocations and DLs inside the TBs. Therefore, annealing at 300 ℃ can cause the annihilation of these dislocations, which result in the slight increase of loop density in TB region.

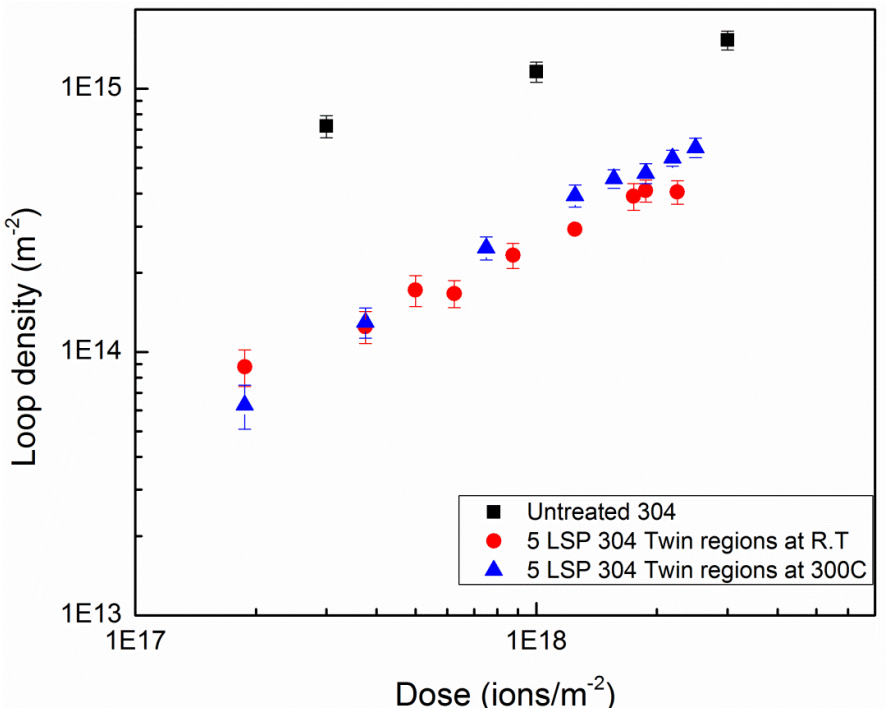

Figure 3.9 Comparison of loop density as a function of dose: untreated sample at r.t is in black rectangles; 5 LSP sample in twin boundary region at r.t is in red circles and 5 LSP sample in twin boundary region at 300℃ is in blue triangles.

3.5 Microstructural evolution of LSP 304 stainless steel in elevated temperature condition

As discussed above, laser shock processing can induce a high density of dislocations, stacking faults and twin boundaries in the 304 stainless steel. However, with the sample annealed to 300℃, microstructural evolution of the LSP sample will take place. As for dislocations, because of the high mobility and recovery behavior at elevated temperatures, annihilation and rearrangement of the LSP generated dislocations occurs and consequently the density of dislocation decreased. The behavior of dislocations in low temperature annealing can alter the LSP effect depending on the material and strengthening mechanism. In the case of AISI 8620, which is a ferritic stainless steel studied by J.Z.Lu et al. about the LSP strengthening and grain refinement mechanism [76], the effect of dislocation annihilation is expected to result in the release of residual stress and the increase of the grain size. The reason is that the grain refinement of the AISI 8620 steels is achieved by formation of dislocation walls. When their laser-peened samples are annealed at 300℃, some of the LSP generated dislocations as well as the dislocation walls are expected to be annihilated. As a result, about 20% of the residual stress will be released. This predication is based on the data from M.R.James [77].

In the case of LSP 304, the microstructural evolution upon annealing will be different because the grain refinement mechanism is based on the formation and intersection of mechanical twins (MTs) instead of dislocation walls, as reported by J.Z.Lu et al. [71]. Along with large numbers of dislocations and SFs, MTs are formed after LSP and they are thermally stable in this temperature regime, as confirmed by Fig.10 and M.Shimada et

al.'s report [78]. The effect of annealing will thus be related to the interaction between dislocations and newly-formed TBs. Many of the mechanisms for dislocations-coherent twin boundary (CBT) interaction have been studied and the application of these mechanisms is based on different materials and types of dislocations. For austenitic steels, both screw and non-screw dislocations can be dissociated by TBs into partial dislocations and when this happens, some of the partial dislocations can pass through or propagate along the CBT while others are absorbed. [79-83]. In the meantime, P. H. Pumphreya et al. used hot stage TEM to show that dislocations were annihilated by high angle grain boundaries at elevated temperature for austenitic stainless steel and the annihilation was achieved by dissociation of the dislocations into partials [84]. As a result, annealing our LSP 304 sample to 300℃ would promote the interaction between the newly formed TBs and the dislocations that lie in the TB region. The dissociation and absorption of dislocations would eventually contribute to the release of strain energy and the decrease of dislocation density.

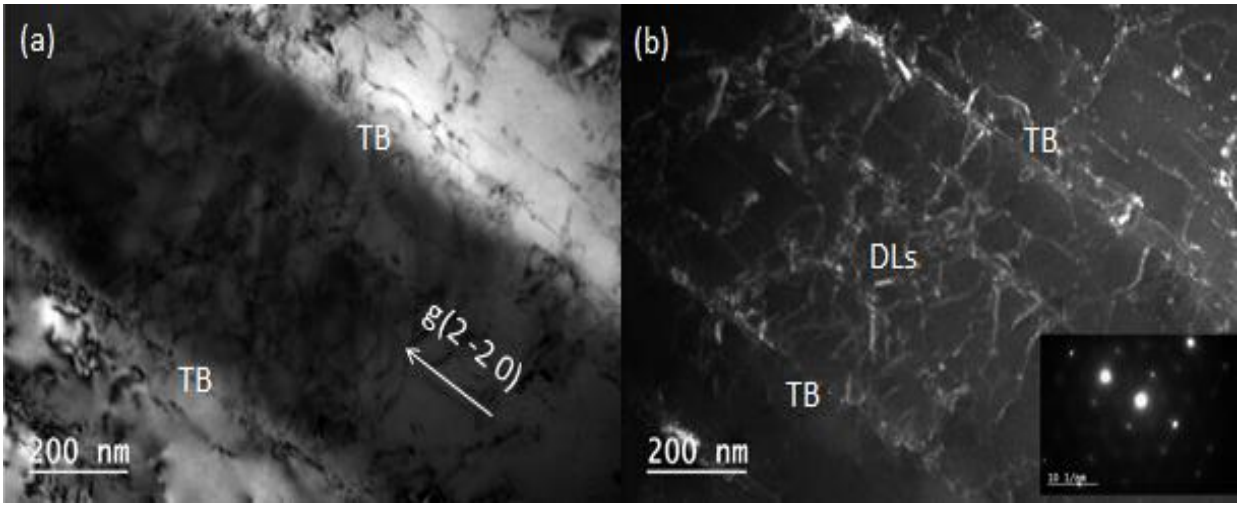

Figure 3.10 TEM images of the 5 LSP sample in TBs region after 300℃ annealing, the beam direction is [112] and g vector is (2 -2 0): (a) is the bright field image; (b) is the dark field image

In both cases (ferritic and austenitic), since the maximum annealing temperature is only 300℃, no grain growth will take place. Note that due to the limitation of laser energy (maximum laser peening energy =850mJ), the grain refinement phenomenon is not significant for the close-peening region. Therefore, the microstructural evolution of the higher energy LSP sample or that at higher elevated temperature will be interesting topics for future investigation.

3.6 Comparison of sink strength for twins and dislocations

While both high density dislocations and TBs can act as sinks for radiation defects, their strength is varied. The concept of sink strength is defined to quantify and compare the different capacity in defect absorption. As determined above in Chapter 3.3, the sink strength of dislocation $(9.14 \pm 1.02) \times 10^{13}\ m^{-2}$, which is approximately $1.0 \times 10^{14}\ m^{-2}$.

Calculation of the TB sink strength is based on the sink strength of grain boundary for point defect, which is shown as followed [85]:

$$S_{GB} = A \times sin\frac{\theta}{2} \quad \text{Eqn. 13}$$

where θ is the misfit angle and A is 2Z/bd. b is the magnitude of the Burger's vector for edge dislocation, i.e. $|b| = \frac{a_0}{2}\sqrt{h^2 + k^2 + l^2}$, and Z/d is defined as the number of point defects extinguished per length of dislocation. From our in-situ irradiation at dislocation region, it is estimated that for a total length of 10 micron dislocation line, there would be around 25 point defects absorbed. The value of Z/d is thus estimated as 2.5×10^6 m^{-1} . To determine the misfit angle, the diffraction pattern of the TB was indexed and shown in Figure 11. From Figure 11, the misfit angle Θ is determined as 70.5 degree. Assuming a_0 equals to the lattice constant of FCC iron (3.65Å), S_{TB} =7.44×10^{15} m^{-2}. Even though the grain structure of our LSP 304 samples remains coarse, the sink strength of the TBs is comparable to the grain boundary sink strength of the ultrafine grained 304L stainless steel [54], which is around 6×10^{15} m^{-2}. A possible explanation is that the generation of high density dislocations and most importantly, the high sink strength of incoherent twin boundaries gives rise to a high capacity to capture radiation-induced point defects. Comparing the sink strength of the LSP generated dislocations and the sink strength of the LSP generated dislocations twin boundaries gives the following relationship: $S_{TB} > S_{dis}$ [86].

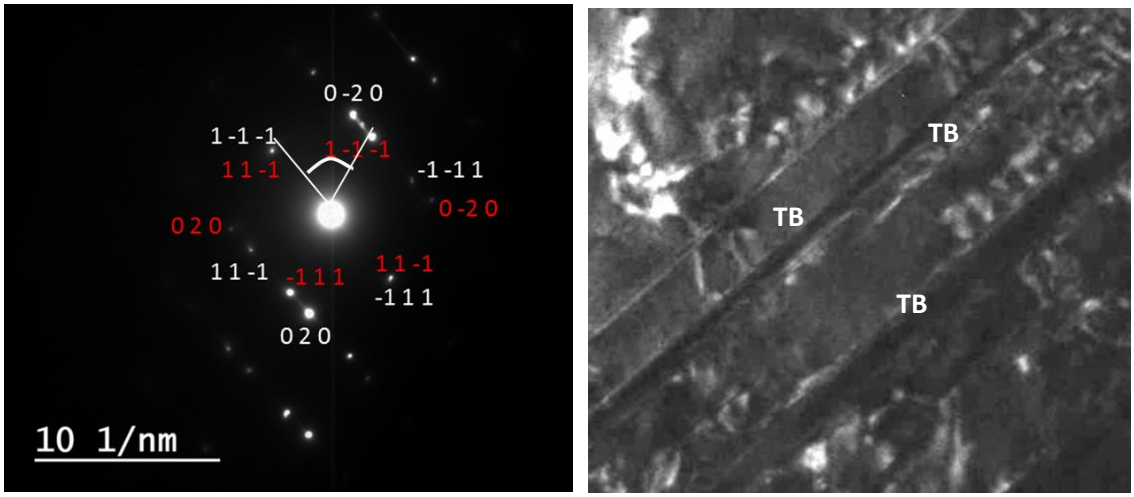

Figure 3.11 Index of the twin boundary diffraction pattern. The beam direction is [1 0 1], g is [-1 -1 1]

3.7 Analysis of the LSP effect on Stress Corrosion Cracking

The untreated 304 stainless and 304 ODS steel samples were subjected to the same stress corrosion environment. It was found that SCC occurred significantly in the untreated 304 stainless and 304 ODS steels. The crack growth rate as a function of stress intensity factor was used to describe the SCC process. To determine this relationship, the crack length as a function of time was firstly determined. As for the 304 stainless steel, the crack initiated at 30 hours and grew until the sample failed at 43 hours. The crack length at every 2.5 hours from 30 to 43 hours was measured by SEM and shown in Figure 3.12. The crack length as a function of time was thus obtained and shown in Figure 3.13 and Figure 3.14. From Figure 3.13, the slope at each point was determined as the crack growth rate or dN/da. With the crack length and applied stress (constant) known, the stress intensity factor can be calculated. The crack growth rate as a function of stress

intensity factor for 304 stainless steel and 304 ODS steel were thus determined and shown in Figure 3.15. Compared with the theoretical curve in Figure 1.16, both SCC in 304 ODS and 304 stainless exhibit a stage I (exponential growth) and stage II (steady state growth). The difference is the crack growth rate in 304 ODS steel is slight higher than 304 stainless steel.

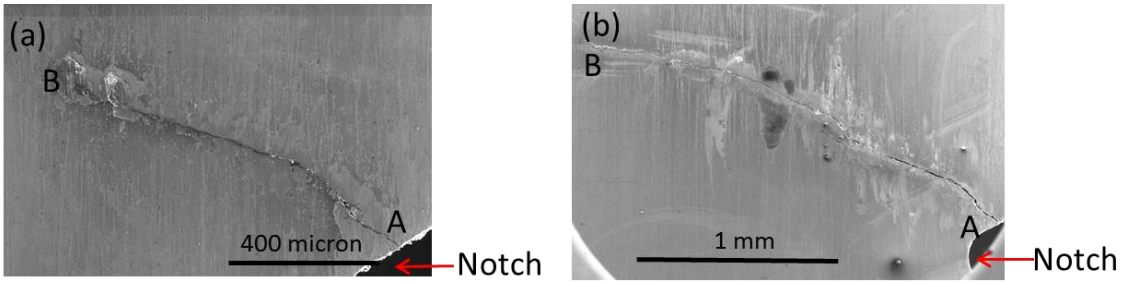

Figure 3.12: Measuring crack length in SEM. Here shows an example of the 304 stainless steel notch sample subjected to SCC at 30 hours and 35 hours. The crack length is the distance from crack tip A to its end B.

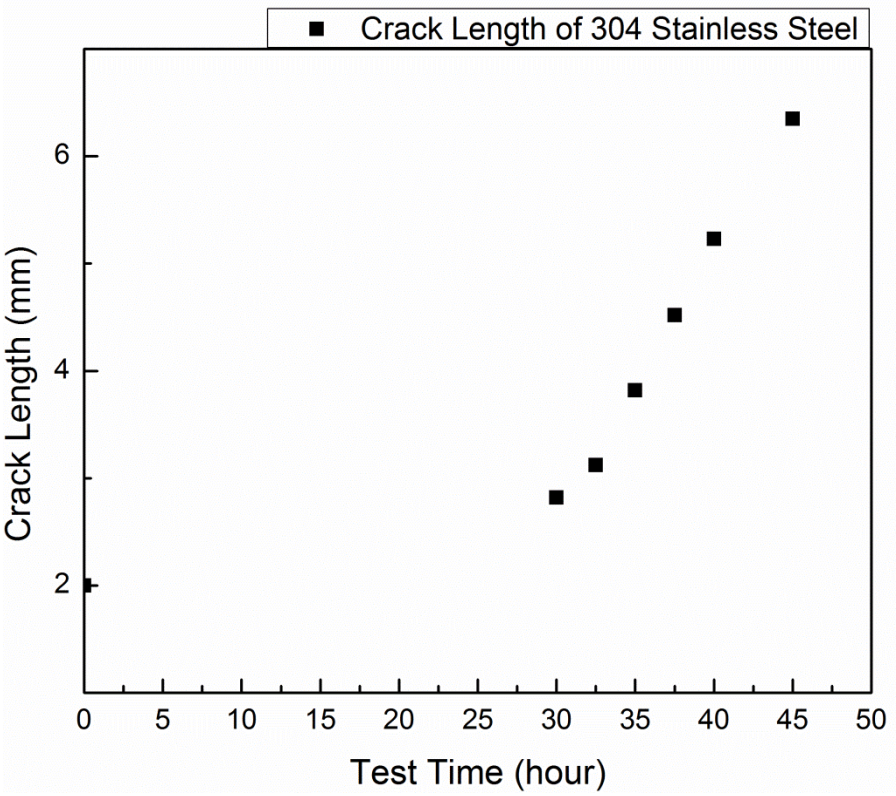

Figure 3.13 Crack length as a function of time for 304 stainless steels

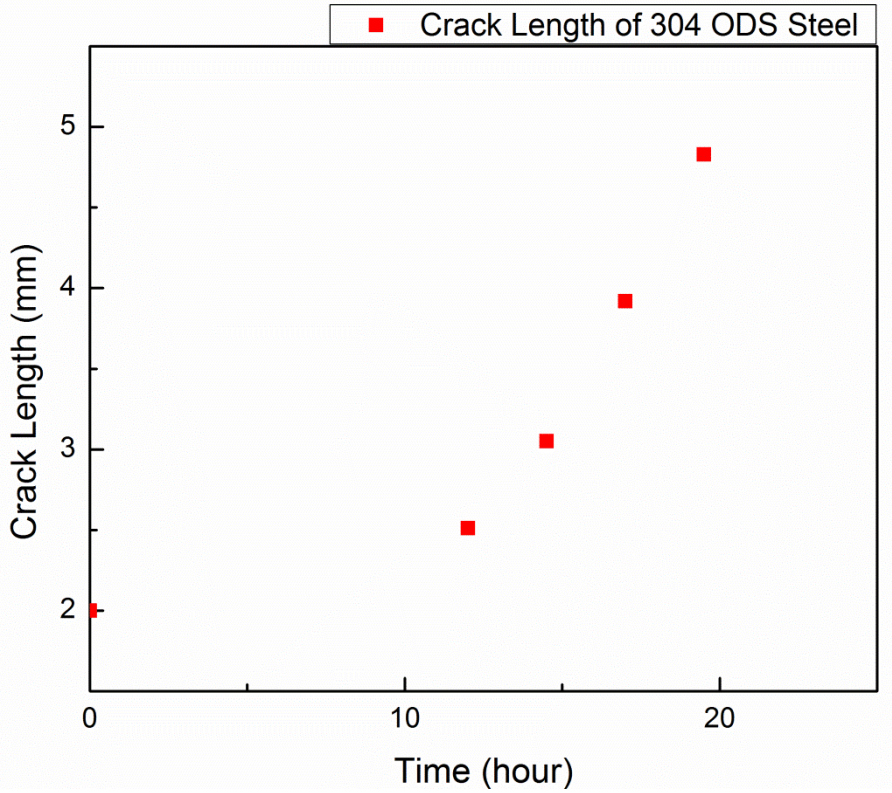

Figure 3.14 Crack length as a function of time for 304 ODS steels

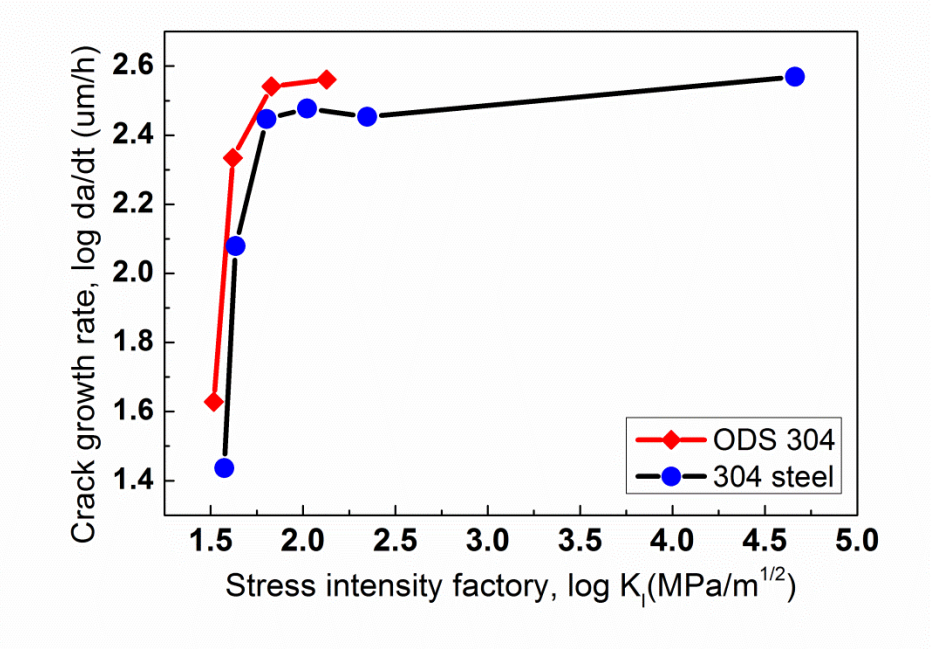

Figure 3.15 Crack growth rate as a function of stress intensity factor.

Optical microscope was used to observe the crack morphology in the cross section of the 304 stainless steels. As Figure 3.16 shows, the crack was firstly initiated along the grain boundary but later propagate across the grain at different direction. Most of the cracks are observed as TGSCC with a small number of IGSCC. This crack morphology is related to the corrosion environment and the applied stress. In this test, the sample was subjected to a saturated $MgCl_2$ solution at boiling point (144℃), with around 200 MPa tensile stress. The applied stress can cause film rupture and break down the protective passive film. Then the solution provides a 'low pH value' (pH = 5) environment by the following electrochemical reaction:

$$Mg^{2+} + 2H_2O \rightarrow Mg(OH)_2 + 2H^+$$

Under this condition, crack will initiate at the rupture sites and propagate across the grain, following the film-induced cleavage model as discussed in the SCC mechanism. As a result, the crack morphology appears as TGSCC, as the model predicts.

However, when the LSP treatment was carried out prior to the SCC test, the LSP samples were found to be much more resistant against SCC. As Figure 3.17 shows, no cracks were observed at the cross-section of the laser peened 304 stainless steels after subjected to the SCC environment for a longer time, 96 hours. Possible reason is that the LSP process can induce compressive stress to the material, which can resist the applied tensile stress and protect the passive film from rupture.

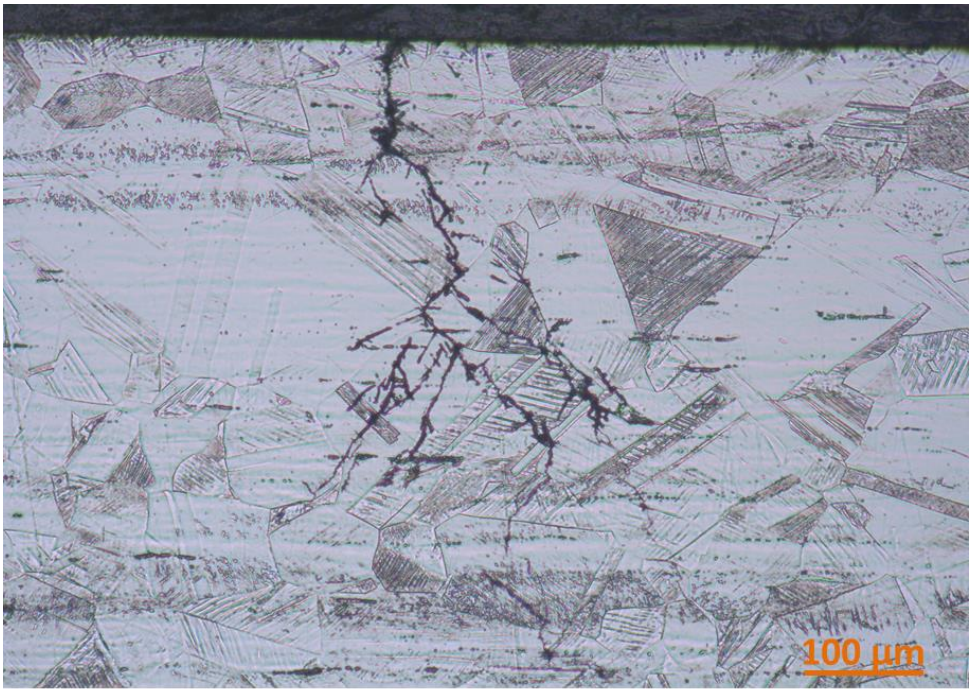

Figure 3.16 Cross-sectional grain morphology of the untreated 304 stainless steel subjected to 72 hours SCC tests. Transgranular and Intergranular cracks were observed.

Figure 3.17 Cross-sectional grain morphology of the laser-peened 304 stainless steel subjected to 96 hours SCC tests. No cracks were observed.

3.8 Future Work

The in-situ irradiation experiment performed in the 304 ODS steel did not reveal a radiation process with high enough resolution for the loop density analysis. A future visit at Argonne National Lab should focus on the irradiation of the laser-peened 304 ODS steels (dark field TEM mode is recommended for observation of point defect clusters). Then comparison of radiation damage of 304 ODS and 304 stainless steels with and without LSP can be achieved.

Laser shock peening with a higher energy laser source is needed in order to induce grain refinement in the austenitic stainless steels – this is important as grain refinement is proved to be effective in resisting radiation damage as well as stress corrosion cracking. If grain refinement can be achieved, a possible grain refinement mechanism can be proposed.

As for stress corrosion cracking, due to the limited amount of ODS materials, whether LSP can have the same SCC resistant effect on ODS has not yet been studied. Further experiments in this part should focus on the investigation of LSP effect on ODS alloy, especially studying the interaction of LSP generated defects with the nano-sized oxide particles and how these interactions can affect the behavior under stress corrosion. In the meantime, it is worthy to determine the crack growth rate as a function of stress intensity factor for the LSP samples and compare them with the untreated one in order to quantify the LSP effect.

CHAPTER 4: CONCLUSIONS

Microstructural evolution of the austenitic stainless steels after laser shock peening treatment was investigated. With the change of microstructure, the laser peened samples were further tested by in-situ irradiation TEM and stress corrosion cracking to study the effect of these LSP induced defects and compressive stress on the materials behavior under heavy ion radiation damage and stress corrosion. The key conclusions include:

1. LSP was found to generate shock waves and produce severe plastic deformation into the austenitic steels. By means of TEM, large numbers of LSP generated twin boundaries (TBs) and dislocation lines (DLs) and stacking faults (SFs) are identified.

2. Irradiation of 304 stainless steel at low temperature regime (< 300 ℃) can generate high density of dislocation loops which appear as white dots in dark-field TEM mode. However, when the samples were subjected to laser peening prior to irradiation, the dislocation loop density was found to decrease as large as one magnitude, which means less radiation damage. Further investigation of the irradiation process shows that high density dislocation and twin boundary can serve as high strength sink for radiation defects. Consequently, LSP process can improve the radiation resistance of austenitic steel by generating high density dislocations and twin boundaries.

3. Stress corrosion cracking was found to occur significantly in 304 stainless and 304 ODS steels. The crack growth rate and stress intensity factor exhibits a similar relationship as the theoretical model except the stage III is missing because of the limited dimension of the material or short last time of stage III. However, when the 304 stainless

steel sample was subjected to LSP treatment prior to SCC test, no apparent cracks were observed even in a longer SCC test time. This indicates laser peening can effectively increase the resistance against stress corrosion in not only crack initiation but also crack propagation.

References:

[1] ASM International. Stainless Steels for Design Engineers Chapter 6.

[2] A.Hirata, T.Fujita, Y.Wen, J.Schneibel, C.Liu, M.Chen. Atmoic structure of nanoclusters in oxide-dispersion-strengthened steels. Nature Materials. 2011.

[3] H.Oka, M.Watanabe, H.Kinoshita, T. Shibayamaa, N. Hashimotoa, S. Ohnukia el at. In situ observation of damage structure in ODS austenitic steel during electron irradiation. Journal of Nuclear Materials. vol.417 2011 pp.279-282

[4] M.Wang, Z.Zhou, H.Sun. H.hu, S. Li Microstructural observation and tensile properties of ODS-304 austenitic steel. Material Science and Engineering:A vol559 2013 pp.287-292

[5] Askar yan CA, Moroz EM. Pressure on evaporation of matter in a radiation beam. *Journal of Experimental and Theoretical Physics Letters* 1963;16:1638–44.

[6] White RM. Elastic wave generation by electron bombardment or electromagnetic wave absorption. *Journal of Applied Physics* 1963;34:2123–4.

[7] Gregg DW, Thomas SJ. Momentum transfer produced by focused laser giant pulses. *Journal of Applied Physics* 1966;27:2787–9.

[8] Skeen CH, York CM. Laser-Induced "blow-off" phenomenon. *Applied Physics Letters* 1968; 12:369–71.

[9] Anderholm NC. Laser-generated stress waves. *Applied Physics Letters* 1970;16:113–5.

[10] Jones ED. Ultrafast laser-induced stress waves in solids. *Applied Physics Letters* 1971;18:33–5.

[11] Fairand BP, Clauer AH, Jung RG, Wilcox BA. Quantitative assessment of laser-induced stress waves generated at confined surfaces. *Applied Physics Letters* 1974;25:431–3.

[12] Fairand BP, Clauer AH. Use of laser generated shocks to improvethe properties of metals and alloys. *Industrial Applications of High Power Laser Technology* 1976;86:112–9.

[13] Fairand BP, Clauer AH, Wilcox BA. Pulsed laser induced deformation in an Fe-3 Wt Pct Si alloy. *Metallurgical Transactions A* 1977;8A:119–25.

[14] Fairand BP, Clauer AH, Wilcox BA. Laser shock hardening of weld zones in aluminum alloys. *Metallurgical Transactions A* 1976;8A:1871–6.

[15] Fairand BP, Clauer AH. Laser generated stress waves: their characteristics and their effects to materials. Presented at Proc.*American Inst. of Physics Conf. on 'Laser Solid Interactions and Laser Processing'*; 1978.

[16] Fairand BP, Clauer AH. Applications of laser-induced stress waves. *Presented at Lasers in Modern Industry Seminar*; 1978.

[17] Clauer AH, Fairand BP. Interaction of laser-induced stress waves with metals. Presented at Proc. *ASM Conference Applications of Lasers in Materials Processing*; Washington DC; 1979.

[18] Henry George Liddell, Robert Scott, *A Greek–English Lexicon*, on Perseus

[19] P. Peyre, L. Berthe, X. Scherpereel, R. Fabbro, Laser-shock processing of aluminium-coated 55C1 steel in water-confinement regime, characterization and application to high-cycle fatigue behaviour, *J. Mater. Sci.33* (1998) 1421–1429.

[20] Kan Ding, Lin Ye. Simulation of multiple laser shock peening of a 35CD4 steel alloy. *Simulation of multiple laser shock peening of a 35CD4 steel alloy* Volume 178, Issues 1–3, 2006, 162–169.

[21] Smartlab stress measurement guideline. Rigaku. Residual Stress Analysis Group

[22] Chu JP, Rigsbee JM, Banas G, Lawrence FV, Elsayed-Ali HE.Effects of laser-shock processing on the microstructure and surface mechanical properties of Hadfield manganese steel. *Metallurgical and Materials Transactions A* 1995;26A:1507–17.

[23] Peyre P, Berthe L, Scherpereel X, Fabbro R. Laser-shock processing of aluminum coated 55C1 steel in water-confinement regime, characterization and application to high-cycle fatigue behaviour. *Journal of Materials Science* 1998;33:1421–9.

[24] Peyre P, Fabbro R, Merrien P, Lieurade HP. Laser shock processing of aluminum alloys. Application to high cycle fatigue behaviour. *Materials Science and Engineering 1996*;A210:102–13.

[25] Masse JE, Barreau G. Surface modification by laser induced shock waves. *Surface Engineering* 1995;11:131–2.

[26] Charles S. Montross a, Tao Wei a, Lin Ye a,∗, Graham Clark b, Yiu-Wing Mai a Laser shock processing and its effects on microstructure and properties of metal alloys: a review

[27] Clauer AH, Koucky JR. Laser shock processing increases the fatigue life of metal parts. *Materials and Processing* 1991;6:3–5.

[28] Peyre P, Berthe L, Scherpereel X, Fabbro R. Laser-shock processing of aluminum coated 55C1 steel in water-confinement regime, characterization and application to high-cycle fatigue behaviour. *Journal of Materials Science* 1998;33:1421–9.

[29] Clauer AH, Holbrook JH, Fairand BP. Effects of laser induced shock waves on metals. In: Meyers MA, Murr LE, editors. *Shock waves and high-strain-rate phenomena in metals. New York: Plenum Publishing Corporation*; 1981. p. 675–702.

[30] Peyre P, Fabbro R, Merrien P, Lieurade HP. Laser shock processing of aluminum alloys. Application to high cycle fatigue behaviour. *Materials Science and Engineering* 1996;A210:102 13.

[31] J.Z. Lu, J.W. Zhong, K.Y. Luo, L. Zhang, F.Z. Dai el at. Microstructual strengthening mechanism of multiple laser shock processing impacts on AISI8620 steel. Material Science and Engineering :A 528 19-20 2011 6128-6133.

[32] J.Z. Lu , K.Y. Luo, , Y.K. Zhang G.F. Sun Y.Y. Gu el at. Grain refinement mechanism of multiple laser shock processing impacts on ANSI 304 stainless steel. *Acta Materialia* Vol.58 16 2010 5354-5362.

[33] Koichi Akita, Yuji Sano, Kazuma Takahashi, Hirotomo Tanaka, Shin Ichi Ohya. Strengthening of Si3N4 Ceramics by Laser Peening. *Materials Science Forum* vol.524-525 2006.

[34] M.Meyers, K. Chawala. Mechanical behavior of materials 2nd edition. Cambridge, 2009.

[35] S.J.Zinkle, L.L.Snead. Designing radiation resistance in materials for fusion energy. *Annual Review of Material Research*. 2014. 44:241-267

[36] B.P.Uberuaga, L.J.Verno, E. Martinez, A.Voter. The relationship between grain boundary structure, defect mobility and grain boundary sink efficiency. *Scientific reports.* (2015) 13

[37] W.Z.Han, M.J.Demkowicz, E.G.Fu, Y.Q.Wang, A.Misra. Effect of grain boundary character on sink efficiency. *Acta Materialia*. 60 (2012) 6341-6351

[38] S.J. Zinkle, P.J.Maziasz, R.E.Stoller. Dose dependence of the microstructural evolution in neutron-irradiated austenitic stainless steel. Journal of nuclear material, 1993.

[39] S.J. Zinkle. Effect of H and He irradiation on cavity formation and blistering in ceramics. *Nuclear Instruments and Methods in Physics Research Section B: Beam Interactions with Materials and Atoms.*vol.286 2012 ppp.4-19

[40] R.G. Carter , N. Soned, K. Dohi, J.M. Hyde, C.A. English el at. Microstructural characterization of irradiation-induced Cu-enriched clusters in reactor pressure vessel steels. *Journal of Nuclear Materials*. vol.298 2001 pp 211-224

[41] J.P. Shepherd. Irradiation-induced precipitation in niobium-stabilized stainless steel. *Journal Name: Metal Sci*. J. 3: 229-34(Nov 1969)

[42] R. K. Williams F. W. WiffenJ. BentleyJ. O. Stiegler. Irradiation induced precipitation in tungsten based, W-Re alloys *Metallurgical Transactions A.* Volume 14, Issue 3, pp 655-666

[43] R. Cauvin and G. Martin. Solid solutions under irradiation. II. Radiation-induced precipitation in AlZn undersaturated solid solutions. *Phys. Rev.* B 23,1981

[44] G. Was, J. Wharry, B. Frisbie. Assessment of radiation-induced segregation mechanisms in austenitic and ferritic–martensitic alloys. *Journal of Nuclear Materials*. vol 411 2011 41-50.

[45] S.J. Zinkle, G.S. Was. Materials challenges in nuclear energy

[46] E. Snoeks, A. Polman and C. A. Volkert. Densification, anisotropic deformation, and plastic flow of SiO2 during MeV heavy ion irradiation. *Appl. Phys. Lett*. 65, 2487 (1994)

[47] S. Som, S. Dutt, Vijay Kumar, Vinod Kumar, H.C. Swart el at. Swift heavy ion irradiation induced modification in structural, optical and luminescence properties of Y2O3:Tb3+ nanophosphor. Journal of Luminescence. vol.146 2014 162-173.

[48] Blas Pedro Uberuaga ⇑, Samrat Choudhury, Alfredo Caro. Ideal sinks are not always ideal: Radiation damage accumulation in nanocomposites. *Journal of Nuclear Materials*. vol 462 2015 402-408.

[49] Yamashita, S., Akasaka, N. & Ohnuki, S. Nano-oxide particle stability of9-12Cr grain morphology modified ODS steels under neutron irradiation. *J. Nucl. Mater*. 3 29-33, 377-381 (2004)

[50] Okuda, T. & Fujiwara, M. Dispersion behavior of oxide particles in mechanically alloyed ODS Steel. *J. Mater. Sci. Lett*. 14, 1600_1603 (1995).

[51] Klimiankou, M., Lindau, R. & Moslang, A. Energy-filtered TEM imaging and EELS study of ODS particles and argon-filled cavities in ferritic-martensitic steels. Micron 36, 1_8 (2005).

[52] Kishimoto, H., Alinger, M. J., Odette, G. R. & Yamamoto, T. TEM examination of microstructural evolution during processing of 14CrYWTi nanostructured ferritic alloys. *J. Nucl. Mater*. 329_33, 369_371 (2004).

[53] Klimiankou, M., Lindau, R. & Moslang, A. HRTEM study of yttrium oxide particles in ODS steels for fusion reactor application. J. Cryst. Growth 249, 381_387 (2003).

[54] C. Sun, S. Zheng, C. C. Wei, Y. Wu, L. Shao, el at. Superior radiation-resistant nanoengineered austenitic 304L stainless steel for applications in extreme radiation environments. Scientific Reports 5. Article number: 7801 (2015).

[55] Brailsford AD, Bullough R. 1972. The rate theory of swelling due to void growth in irradiated metals. *J. Nucl. Mater*. 44:121–35

[56] Johnson RA, Lam NQ. 1976. Solute segregation in metals under irradiation. *Phys. Rev. B* 13:4364–75

[57] Adda Y. 1972. Report on the CEA program of investigations of radiation-induced cavities in metals: presentation of some results. In Radiation-Induced Voids in Metals, ed. JW Corbett, LC Ianniello, pp. 31–81. Springfield, VA: Natl. Tech. Inf. Serv

[58] Brager HR. 1975. The effects of cold working and pre-irradiation heat treatment on void formation in neutron-irradiated type 316 stainless steel. J. Nucl. Mater. 57:103–18

[59] Bloom EE, Stiegler JO. 1970. A comparison of irradiation-induced swelling and void formation in two austenitic stainless steels. J. Nucl. Mater. 35:244–46

[60] A.Cohen Copper Development Association

[61] B.E. Wlide, Metals Handbook, Failure Analysis, ASM International

[62] D.A. Jones. Principles and Prevention of Corrosion. 2nd Edition

[63] ASM International, Metals Handbook (Desk Edition) Chapter 32 (Failure Analysis), American Society for Metals, (1997) pp 32-24 to 32-26

[64] Jarmila Woodtli, Rolf Kieselbach Damage due to hydrogen embrittlement and stress corrosion cracking. *Engineering Failure Analysis* 7 (2000) 427-450

[65]J.F. Newman. Corrosion Science: The stress corrosion of steel in sodium hydroxide solution: a film-rupture model. Corrosion Science Vol 21, Issue 7, 1981, Pp 487-503

[66] X. Mao , D. Li. Slip-step dissolution and micromechanical analysis to model stress-corrosion crack growth of type 321 stainless steel in boiling magnesium chloride. Metallurgical and Materials Transactions A. 1995, Volume 26, Issue 3, pp 641-646

[67] Struer. Instruction Manual of Twin-jet-polishing machine

[68] D.B.William, C.B.Carter .Transmission Electron Microscopy, a textbook for material science. Springer

[69] Z. Yao, M. Hernández-Mayoral, M.L. Jenkins & M.A. Kirk. Heavy-ion irradiations of Fe and Fe–Cr model alloys Part 1: Damage evolution in thin-foils at lower doses. Philosophical Magazine. Volume 88, Issue 21, 2008

[70] Cortest. Instruction Manual of Proof Ring System.

[71] J.Z. Lu, K.Y.Luo, Y.K.Zhang, G.F.Sun, Y.Y.Gu, J.Z. Zhou et al. Grain refinement mechanism of multiple laser shock processing impacts on ANSI 304 Stainless steel. Acta Materialia 58(2010), pp. 5354-5362

[72] C.Sun, S.Zheng, C.C. Wei, Y.Wu, L.Shao, Y.Yang et al. Superior radiation-resistant nanoengineered austenitic 304L stainless steel for applications in extreme radiation environments. Scientific Reports. (2015) Jan 15;5:7801

[73] G.S. Was, Fundamentals of Radiation Materials Science, Springer, Berlin, 2007.

[74] W.Z.Han, M.J.Demkowicz, E.G.Fu, Y.Q.Wang, A.Misra. Effect of grain boundary character on sink efficiency. *Acta Materialia*. 60 (2012) 6341-6351.

[75] B.P.Uberuaga, L.J.Verno, E. Martinez, A.Voter. The relationship between grain boundary structure, defect mobility and grain boundary sink efficiency. *Scientific reports.* (2015) 13 March

[76] J.Z.Lu J.W.Zhong, K.Y.Luo, L.Zhang, F.Z.Dai, K.M.Chen et al. Micro-structural strengthening mechanism of multiple laser shock processing impacts on AISI 8620 steel. Materials Science and Engineering A. 528(2011) 6128-6133.

[77] M.R.James. Relaxation of residual stresses an overview. Proceedings of the28th Sagamore Ar my Materials Research Conference. (1982) 297–314.

[78] M.Shimada, H.Kokawa, Z.J.Wang, Y.S.Sato, I.Karibe. Optimization of grain boundary character distribution for intergranular corrosion resistant 304 stainless steel by twin-induced grain boundary engineering. Acta Materialia 50(2002) 2331-2341

[79] Y.J.Li, X.H.Zeng, W.Blum. Transition from strengthening to softening by grain boundaries in ultrafine-grained Cu. Acta Materialia. 52(2004) 5009-5018

[80]N.Li, J.Wang, A.Misra,X.Zhang, J.Y.Huang, J.P.Hirth. Twinning dislocation multiplication at a coherent twin boundary. 59 (2011) 5989-5996

[81]R.C.Pond, D.A.Smith. On the absorption of dislocations by grain boundaries. Philosophical Magazine. 36 (1977) 353-366

[82]Z.H.Jin, P.Gumbsch, E.Ma, K.Albe, K.Lu, H.Hahn, H.Gleiter. The interaction mechanism of screw dislocations with coherent twin boundaries in different face-centered cubic metals. Scripta Materilia 53(2006) 1163-1168.

[83] Z.H.Jin, P.Gumbsch, E.Ma, K.Albe, K.Lu, H.Hahn, H.Gleiter. Interactions between non-screw lattice dislocations and coherent twin boundaries in face-centered cubic metals. Acta Materialia 56(2008) 1126-1135.

[84] P. H. Pumphreya & H. Gleitera. The annealing of dislocations in high-angle grain boundaries. Philosophical Magazine. 30 (1974) 593-602.

[85] S. Watanabe, N. Sakaguchi, N. Hashimoto, H. Takahashi. Sink effect of grain boundary on radiation-induced segregationin austenitic stainless steel. Journal of Nuclear Materials. (2000) 152-156

[86] S. Watanabe, N. Sakaguchi, N. Hashimoto, H. Takahashi. Quantitative studies of irradiation-induced segregation and grain boundary migration in Fe-Cr-Ni alloy. Journal of Nuclear Materials. 224 (1995) 158.